Journal of Materials Chemistry A

ROYAL SOCIETY OF CHEMISTRY

PAPER

View Article Online
View Journal | View Issue

Cite this: J. Mater. Chem. A, 2021, 9, 15415

Tuning of Pt–Co nanoparticle motifs for enhancing the HOR performance in alkaline media†

D. J. Weber,[ab] C. Dosche [b] and M. Oezaslan [*ab]

For a future sustainable hydrogen economy, the electrocatalysis of hydrogen oxidation/evolution reactions (HOR/HER) needs to be better understood. In order to describe the strong alteration of HOR/HER rates on platinum group metals (PGM) in acidic and alkaline media, at least two prominent descriptors based on a Pt–H_{ad} binding energy model and a bifunctional model are frequently discussed in the literature. A clear discrimination of these both descriptors for PGM-based multi-metallic materials, yet, remains a critical challenge. To solve this dilemma, we have made use of the oxophilic and structural properties of cobalt atoms in Pt-based nano-materials to tune their catalytic HOR performance in alkaline media. More precisely, we have designed Pt_xCo_{1-x} nanoparticles with various structural motifs. Remarkably, the surface rearrangement of Pt_xCo_{1-x} nanoparticles along the uniform alloy, Pt-rich shell, and Co-segregated core–shell motifs is controlled by the electrochemical environment. To identify the elemental distribution of Co and Pt atoms, a new descriptor is presented in this work, the so-called $Q(Hupd)/Q(Co^{z+})$ ratio. The coverage of OH_{ad} species can be controlled by the coverage of oxophilic Co surface atoms to investigate the bifunctional mechanism on the HOR kinetics in alkaline media. Thus, we are able to correlate the HOR exchange current densities with tuneable Co coverage on the particle surface to mimic *e.g.* the coverage of "Co(hydr)oxide clusters". On the other hand, the strain effect to modify the Pt–H_{ad} binding energy is solely investigated on a Pt-rich shell induced by a Co-rich particle core. Despite the separation of these critical model parameters, cobalt as an oxophilic component strongly bonds OH_{ad} species at the bimetallic particle surface and modifies the HOR kinetics. In contrast, the induced lattice strain in the Pt-enriched shell of dealloyed core–shell nanoparticles leads to an increase of the Pt surface area-based specific exchange current density j^0_{spec} by a factor of ~2 compared to pure Pt. Based on our results, we provide deeper insights into the kinetics and mechanism of the HOR on Pt_xCo_{1-x} catalysts with different structural nanoparticle motifs in an alkaline environment.

Received 10th March 2021
Accepted 10th June 2021

DOI: 10.1039/d1ta02067f

rsc.li/materials-a

Introduction

The electrocatalysis of hydrogen oxidation/evolution reactions (HOR/HER) is the main key for the hydrogen economy to meet the demands of renewable and clean energy conversion and energy storage in the near future. The hydrogen electrocatalysis is not only a fundamental research in academia. Actually, there are numerous industrial technologies in the field of water and chlor-alkali electrolysis,[1,2] fuel cells, metal deposition,[3] and corrosion.[4] Both hydrogen reactions have very recently experienced a renaissance. Although the HOR/HER have been studied over decades, their mechanism and kinetics are still poorly understood to date. In particular, the alteration of their reaction rate from acidic to alkaline environments is dramatic. Very low loadings of platinum group metals (PGM) are needed to accelerate the HOR kinetics in proton exchange membrane fuel cells,[5] whereas the same reaction at higher pH becomes at least two order of magnitudes slower.[6] Improvements in HOR/HER activities have recently been achieved by adding other metals such as ruthenium (Ru) or nickel (Ni) to platinum.[7–12] The origin of the activity improvement especially in an alkaline environment is intensively and controversially discussed in the electrocatalysis community.

One of the important descriptors for the HOR/HER rates is the M–H_{ad} binding energy on the metal electrode surface.[6,13–15] Some studies have also reported that the higher Pt–H_{ad} binding energy in alkaline media is caused by the shortening of the Pt–H_{ad} bond distance compared to that in acidic media.[16–18] Sheng *et al.*[14] have shown a nearly linear dependence of the HOR/HER activity on the pH value of buffered electrolyte solutions. Interestingly, they correlated the shift of the underpotential deposition of hydrogen (Hupd) features measured in cyclic voltammetry (CV) directly with the strengthening/lowering of the Pt–H_{ad} binding energy at different pH values. The Pt–H_{ad}

[a]Technical Electrocatalysis Laboratory, Institute of Technical Chemistry, Technical University of Braunschweig, 38106 Braunschweig, Germany. E-mail: m.oezaslan@tu-braunschweig.de

[b]Institute of Chemistry, University of Oldenburg, 26129 Oldenburg, Germany

† Electronic supplementary information (ESI) available. See DOI: 10.1039/d1ta02067f

binding energy established from the CV profiles increases with pH, resulting in a decrease of the HOR/HER activity. The contribution of OH^- species in the reaction path *via* adsorption has mainly been excluded by the authors. Durst *et al.*[6] have also shown that the ratio of the HOR/HER rates at pH ≈ 0 and pH ≈ 13 varies between 120 and 200, which confirms the order of magnitude of the exchange current density difference in acidic and alkaline environments. If the H binding energy is linearly proportional to the activation energy (as described in the Brønsted–Evans–Polany relationship[19]), they assumed that the Volmer step is the rate limiting step for the HOR/HER on pure Pt in alkaline media.

Besides the theory of $M–H_{ad}$ binding energy, an additional critical descriptor for HOR/HER rates is the interfacial structure of water molecules near the electrode surface reported by Ledezma-Yanez *et al.*[20] They proposed that the interfacial water structure correlates with the pH value and thus affects the energy of hydrogen adsorption. In other words, the transfer of charge (H^+ in an acid or OH^- in a base) through the interfacial double layer depends on the extent to which the solvation environment can accommodate this charge migration. Thus, if the interfacial water can be easily rearranged, the transfer of charge through the double layer is fast. In contrast, a rigid and stiff interfacial water structure impedes and slows down the migration of charge. The extent of water reorganization is strongly related to the position of the potential of zero charge (pzc) as described by the interfacial electric field between the electrode and electrolyte. The pzc shifts from the Hupd region at low pH to a more anodic potential region of Pt (hydr)oxide formation at high pH.[21] As a consequence, the strength of the electric field and the energy associated with the arrangement of interfacial water molecules are strongly influenced by the pH. Due to the pzc shift towards more anodic potentials on a Pt surface, the adsorption rate of hydrogen in the Hupd region is very sluggish in an alkaline environment. Ledezma-Yanez *et al.*[20] have also shown that the introduction of Ni clusters on a Pt(111) surface is able to modify the electric field and results in a shift of the pzc free charge of −25 mV which is closer to the Hupd region. This shift of the pzc free charge leads to improved HER kinetics in alkaline media. Both descriptors, metal–hydrogen binding energy and rearrangement of interfacial water, are strongly linked to the electronic properties of the catalyst surface for the HOR/HER.

Another important descriptor of the HOR/HER rates is the bifunctional mechanism, in which reactive OH_{ad} species might promote the oxidation of H_{ad} on Pt sites according to the Volmer step ($M–H_{ad} + OH^- \rightarrow M + H_2O + e^-$). Strmcnik *et al.*[22] suggested that the adsorption of reactive OH^- species in the Hupd region might dictate the HOR/HER activity on a PGM surface. They have correlated the HOR/HER performance with the oxophilic properties of the PGM-based catalysts and shown that the HOR activity increases in the order of $Pt < Pt_{0.5}Ru_{0.5} \ll Pt_{0.1}Ru_{0.9}$ = polycrystalline Ir in an alkaline environment.[22] Further studies from the same group have reported a critical interplay between the energetics of $Pt–H_{ad}$ and $Pt–OH_{ad}$ to control the HOR/HER rates.[23–25] For instance, Danilovic *et al.*[23] have shown that the modification of the Pt surface with $Ni(OH)_2$ clusters improves the HER activity on Pt. They have suggested that the $Ni(OH)_2$ clusters play an important role in accelerating the dissociative adsorption of water and in supplying the production of hydrogen and hydroxyl intermediates during the HER in alkaline media.

Altogether, different models like $M–H_{ad}$ binding energy, an interfacial structure of water molecules and/or bifunctional mechanism by forming "reactive" OH species are drawn on to describe the changes in HOR/HER kinetics from an acidic toward an alkaline environment. It is noticed that most factors to describe the HOR/HER kinetics are very difficult to separate from each other and often occur together. Moreover, the diffusion of OH^- species, mechanistic formation pathway of OH_{ad}, $OH_{ad}–H/H_{ad}–OH$ bond formation, water desorption step,[26] interactions of alkali cations[27] and water at the electrode–electrolyte interface might also play a role in HOR/HER kinetics, but less studied or still unexplored to date.

In this work, Pt_xCo_{1-x} catalysts along the uniform alloy, Pt-rich shell and Co-segregated core–shell nanoparticle motifs have been investigated for the HOR in alkaline media. The surface structure and re-arrangement of Pt_xCo_{1-x} catalysts are controlled by the electrochemical environment. The changes in HOR exchange current densities on the Pt_xCo_{1-x} catalysts in their different nanoparticle motifs were investigated and related to the strain effect (reduced Pt–Pt distances) and/or bifunctional effect. Due to the high oxophilic character of Co, the surface and subsurface layers of the bimetallic nanoparticles are systematically modified to control the coverage of OH_{ad} species. A new descriptor will be presented to determine the atomic composition and distribution of Co and Pt at the bimetallic particle surface. Very remarkably, in a series of different particle morphologies and compositions, the compressive strain as well as the bifunctional mechanism can be distinguished from each other and allow studying the HOR/HER kinetics in a unique manner. Despite the separation of these critical parameters, cobalt as an oxophilic component strongly bonds OH_{ad} species at the bimetallic particle surface. On the other hand, the induced lattice strain in the Pt-enriched shell of dealloyed core–shell nanoparticles causes only a moderate lowering of the Pt–H binding energy and thus improved HOR activity in alkaline media.

Experimental part

Synthesis of Pt_xCo_{1-x} alloy nanoparticles supported on high surface area carbon (HSAC)

High surface area carbon (HSAC) supported Pt_3Co, PtCo, and $PtCo_3$ alloy nanoparticles were prepared by using a liquid impregnation–freeze drying–reductive thermal annealing technique.[28,29] 50 mg of commercially available 28.4 wt% Pt/HSAC (Tanaka Kikinzoku International Inc, TKK) was added to 35 mg, 105 mg, and 316 mg of $Co(NO_3)_2 \cdot 6H_2O$ (99.999% metal basis, Alfa Aesar) for the preparation of Pt_xCo_{1-x} with atomic Pt : Co ratios of 3 : 1, 1 : 1, and 1 : 3, respectively. First, the cobalt precursor salt was dissolved in around 3 mL of highly purified water (18 MΩ cm at room temperature, Elga Purelab Classic). After horn-sonication for 5 minutes, the viscous black

slurry was immediately frozen in liquid nitrogen for 20 minutes and then freeze-dried in a vacuum for two days. The dried powder was then annealed in a three-zone tube furnace in a 5/95 vol% H_2/Ar atmosphere (quality 5.0, Air Liquide) with a flow rate of 200 mL min^{-1}. The temperature program consisted of two plateaus at 250 °C for two hours followed by at 800 °C for six hours with a heating rate of 10 °C min^{-1}, respectively.

Electrochemical experiments using the thin-film rotating disc electrode (TF-RDE) technique

Preparation of thin catalyst film electrodes. About 3 mg of catalyst powder was mixed with 5 mL purified water (18 MΩ cm at room temperature, Elga Purelab Classic), resulting in a concentration of *ca.* 0.2 g_{Pt} L^{-1}. After horn-sonication for 30 min, an aliquot of 10 μL from the catalyst dispersion was pipetted onto a previously clean and polished surface of a glassy carbon (GC) electrode (outer diameter of 5 mm, Pine Research Instrumentation) and then dried at 40 °C for 15 min in air. The calculated loading was ~8 μg_{Pt} cm_{geo}^{-2} (normalized to the geometric surface area). The GC electrodes were previously polished with 0.05 μm aluminum oxide powder (Buehler) onto a Microcloth polishing cloth (Buehler) until a mirror-like surface has been obtained. The polished GC electrodes were washed in purified water, propan-2-ol (Fisher Chemica, HPLC), and purified water each for 5 minutes using an ultra-sonication bath.

Electrochemical measurements. The electrochemical set-up consisted of a home-made electrochemical three-compartment glass cell, a potentiostat (VSP300, Biologic), and a RDE rotator (Pine Research Instrumentation). A three-electrode-configuration consisted of a Pt mesh as the counter electrode, mercury–mercury oxide (MMO) as the reference electrode, and Pt_xCo_{1-x} catalyst materials as the thin film working electrode, respectively. 0.1 M KOH (99.98%, Alfa Aesar) and 0.1 M $HClO_4$ (70 vol%, 99.999%, Sigma Aldrich) as electrolyte solutions were freshly prepared by dissolving/diluting their respective amount in highly purified water. All potentials reported in this paper were converted into the reversible hydrogen electrode (RHE) scale. The quality of pure Ar and H_2 (Air Liquide) was 99.999% (5.0), respectively.

Cyclic voltammetry (CV). Pt_xCo_{1-x} catalysts as thin films were first cleaned by CV between 0.05 and 1.00 V *vs.* RHE with a scan rate of 50 mV s^{-1} in Ar-saturated 0.1 M $HClO_4$ or KOH, respectively, until a steady-state CV profile has been achieved. The electrochemically active Pt surface area (ECSA) was determined from the hydrogen underpotential deposition (Hupd) region by integrating the hydrogen ad-/desorption region after double layer current correction, assuming a pseudo-capacity of 210 μC cm_{Pt}^{-2} for polycrystalline Pt. The Hupd [cm_{Pt}^2] was normalized by the theoretical Pt mass used to express the ECSA [m^2 g_{Pt}^{-1}].

Linear sweep voltammetry (LSV). The electrolyte was exchanged and saturated with hydrogen by bubbling through the solution for at least 10 minutes before each HOR/HER polarization measurement. LSV profiles were recorded by changing the potential from −0.05 to 0.40 V *vs.* RHE at 10 mV s^{-1} and 1600 rpm (revolutions per minute). The kinetic current densities are calculated by using the Koutecky–Levich equation:

$$\frac{1}{j} = \frac{1}{j_{kin}} + \frac{1}{j_D} \quad (1)$$

where j is the measured current density [mA cm^{-2}], j_{kin} – the kinetic current density [mA cm^{-2}], and j_D – the diffusion-limited current density [mA cm^{-2}]. The HOR/HER polarization measurements were fitted by using the Butler–Volmer equation to extract the exchange current density (j^0) and transfer coefficient (α) [$0 \leq \alpha \leq 1$] from:

$$j = j^0\left(e^{\frac{\alpha F}{RT}\eta} - e^{-\frac{(1-\alpha)F}{RT}\eta}\right) \quad (2)$$

where η is the overpotential [V], F – Faraday constant [96 485.3 A s mol^{-1}], T – temperature [K], and R – gas constant [8.314 J mol^{-1} K^{-1}].

Structural characterization

High resolution transmission electron microscopy (HR-TEM). A JEOL 2100F TEM (operated with an accelerating voltage of 200 kV) was employed to determine the morphology, structure, and mean particle size of pristine and treated Pt_xCo_{1-x} catalysts. Catalyst dispersion in a water/propan-2-ol mixture was pipetted onto a holey carbon film-coated Cu grid (400 mesh) and dried in air. The TEM micrographs were evaluated by using ImageJ 1.51f software.

Energy-dispersive X-ray spectroscopy (EDX). A Hitachi S-3200N scanning electron microscope (SEM) equipped with a cold field emitter and EDX detector (INCA, Oxford Instruments) was employed to analyze the chemical composition of pristine and electrochemically treated Pt_xCo_{1-x} catalysts. The microscope was operated at an acceleration voltage of 20 kV, a beam current of 0.4 nA, 1500× magnification and a working distance of 15 mm. The total acquisition time for each EDX spectrum was around 60 s. The characteristic energy intensities of the L_α-line for Pt and the K_α-line for Co were used for quantification, respectively.

Thermogravimetric analysis (TGA). The total metal content for pristine catalysts was determined by using STARe System TGA (Mettler-Toledo GmbH). 2–3 mg of catalyst powder was transferred into a crucible, loaded onto a thermo-balance and oxidized in synthetic air (99.99%, Air Liquide) at a constant flow rate of 2 mL min^{-1}. The temperature program consisted of three steps: first, the temperature was increased up to 250 °C with 40 °C min^{-1} and held for 5 minutes. The oven temperature was then raised from 250 to 650 °C at 7 °C min^{-1} and held for 6 h. To oxidize the residual graphitized carbon, the temperature was increased up to 900 °C and held for an additional 5 minutes. The accurate Pt loading was calculated from the total metal content *via* TGA and the atomic Pt : Co ratio *via* EDX data.

X-ray diffractometry (XRD). XRD data were acquired by using an Empyrean Theta-Theta diffractometer (Panalytical) equipped with a Cu K_α tube (λ = 1.45 Å, operated at 40 kV and 40 mA), a Bragg–Brentano unit and a position-sensitive PIXCEL 1D

detector (PSD) in a 2θ range of 10–90°, step size of 0.013°, counting time of 700 s, divergence slit of 4 mm, and PSD Iris anti-scattering slit of 7.5 mm. The total acquisition time was around 5 h. The catalyst powder was filled in a commercial sample holder. The depth and diameter of the sample area were 1 mm and 10 mm, respectively. Vegard's law which describes the linear dependence on the lattice parameter of the alloy with those lattice parameters of single components was applied to determine the stoichiometric composition of disordered alloy crystal phases.

X-ray photoelectron spectroscopy (XPS). An ESCALAB 250 Xi spectrometer (Thermo Fisher) with monochromatized Al K_α radiation (1486.6 eV) was employed. Data analysis was performed by using Avantage software (version 5.982). Details about the acquisition parameters are listed in Table S2 of the ESI.† The binding energies were corrected by calibrating the C 1s signal at 284.6 eV. The pristine catalysts were measured as powder, while the electrochemically treated Pt_xCo_{1-x} catalysts were washed off from the surface of the GC electrode, dispersed in a water–propan-2-ol mixture and dropped onto a silicon wafer (Micro-Chemicals, 300 ± 10 μm of thickness).

Results and discussion

Structural characterization of pristine Pt_xCo_{1-x} alloy nanoparticle electrocatalysts

The as-prepared Pt_xCo_{1-x} nanoparticles supported on high surface area carbon (HSAC) were structurally characterized by using HR-TEM, XRD, and EDX. Fig. 1 displays the HR-TEM micrographs of all three Pt_xCo_{1-x} catalysts, showing that the particles are well-dispersed on the carbon support material. Particle agglomeration was not observed from the TEM data. The particle size distribution and mean particle size of pristine Pt_xCo_{1-x} catalysts (Fig. 1d–f) were established by analyzing more than 300 particles from several HR-TEM micrographs. In summary, the mean particle sizes are 3.8 ± 0.8 nm, 4.2 ± 0.9 nm, and 4.4 ± 1.0 nm for pristine Pt_3Co, PtCo, and $PtCo_3$, respectively. Based on the EDX analysis, the atomic Pt : Co ratios were found to be 72 : 28, 47 : 53 and 24 : 76 (standard deviations of 4–5 at%) and are in good agreement with the amount of Co used in the synthetic route for the preparation of bimetallic nanoparticles with desired ratios. This observation and our previous studies[28–31] point out the high robustness and good reproducibility of the wet impregnation–freeze drying–annealing route to prepare uniform alloy nanoparticles.

The XRD patterns of Pt_xCo_{1-x} catalysts are displayed in Fig. S1 of the ESI.† The reflexes at 2θ values of around 40°, 48°, 71°, and 86° correspond to the formation of a disordered face centered cubic (fcc) Pt–Co alloy phase with a space group of $Fm\bar{3}m$. Ordered alloy or oxide phases were not detected by XRD. The formation of ordered alloy phases can be suppressed by quenching during the annealing process from 800 °C to room temperature.[31] The calculated crystallite sizes for Pt_xCo_{1-x} are similar to the mean particle sizes obtained from the TEM data. Based on the Rietveld quantification, the pristine Pt_3Co catalyst appears as a single disordered fcc alloy crystal phase with a stoichiometric composition of $Pt_{84}Co_{16}$ according to Vegard's law. However, the pristine PtCo and $PtCo_3$ catalysts exhibit two crystal phases. The major crystal phase for the PtCo catalyst is a Pt-rich disordered fcc alloy phase, while the $PtCo_3$ catalyst mainly consists of $Pt_{53}Co_{47}$ as the major phase. Table S1† summarizes the obtained crystallite sizes, lattice parameters, results from Rietveld quantification, and stoichiometric compositions for pristine Pt_xCo_{1-x} alloy nanoparticles. It is noted that the EDX results reflect the average composition of

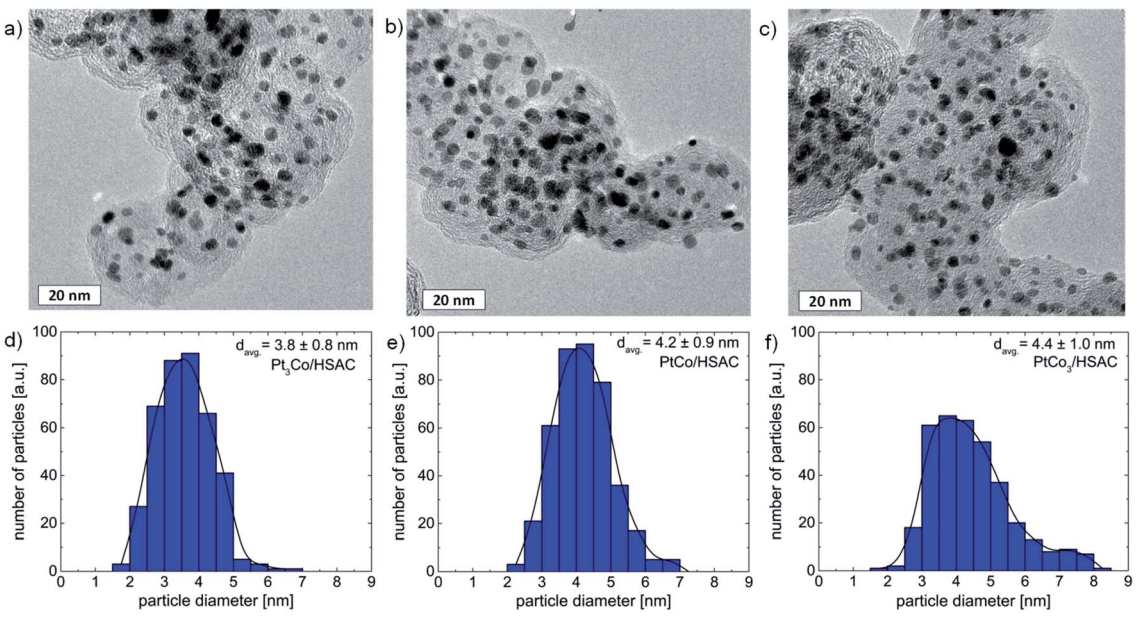

Fig. 1 HR-TEM micrographs and particle size distributions for pristine Pt_3Co (a and d), PtCo (b and e), and $PtCo_3$ (c and f) prepared by the wet-impregnation–freeze drying–annealing route. The scale bar for all HR-TEM micrographs is 20 nm, respectively.

particle ensembles, while the XRD analysis involves the structure and composition of each crystal phase. This leads to different results in the chemical composition of alloy nanoparticles.

Surface-rearrangement of Pt_xCo_{1-x} electrocatalysts along the alloy, Pt-rich shell and Co-segregated core-shell nanoparticle motifs

The surface structure and chemical composition of Pt_xCo_{1-x} alloy nanoparticles can be controlled by the (electro)chemical reaction environment. In principle, cobalt atoms are rapidly dissolved by exposure to a strong acid. On the other hand, cobalt can be (electro)chemically stabilized by forming cobalt (hydr)oxide species, such as $Co(OH)_2$, Co_3O_4, CoOOH, and $Co(OH)_3$, depending on the potential and pH applied. The potential stability together with the proton activity of the cobalt–water system is thermodynamically predicted in the Pourbaix diagram.[32,33] Moreover, its enhanced oxophilic character tends to migrate internal Co atoms from the deeper subsurface layers towards the surface compared to platinum.[34,35]

This unique electrochemical behaviour of cobalt inspired us to take advantage of the adsorbate-induced surface rearrangement of nano-sized Pt_xCo_{1-x} alloys to tailor their catalytic HOR/HER performance in alkaline media. Fig. 2 illustrates our approach to tune the structure of bimetallic Pt_xCo_{1-x} catalysts along the uniform alloy, Pt-rich shell and Co-segregated core–shell nanoparticle motifs controlled by the electrochemical conditions. Very importantly, the initial chemical surface composition and structure of pristine Pt_xCo_{1-x} catalysts in the first surface layers can facilely be probed by recording *in situ* cyclic voltammetry (CV) profiles in alkaline media and *ex situ* X-ray photoelectron spectroscopy (XPS).

Fig. 3a displays the CV profiles of pristine Pt_xCo_{1-x} alloy catalysts in Ar-saturated 0.1 M KOH. The electrochemical features of pristine $PtCo_3$ (blue line), PtCo (orange), and Pt_3Co (green) show the appearance of both metal atoms at the particle surface. To better assign the features to the bimetallic surface, we will briefly describe the characteristics of a pure Pt surface (dashed lines, Fig. 3). The ad/desorption of hydrogen on a Pt surface referred to as underpotential hydrogen deposition (Hupd) occurs between 0.05 and 0.40 V *vs.* RHE, while at potentials above 0.65 V the Pt surface is electrochemically oxidized by forming (hydr)oxide species. The transition from the hydrogen coverage to (hydr)oxide takes place *via* the capacitive double-layer region (0.40–0.65 V *vs.* RHE). As Co atoms co-appear at the particle surface, additional

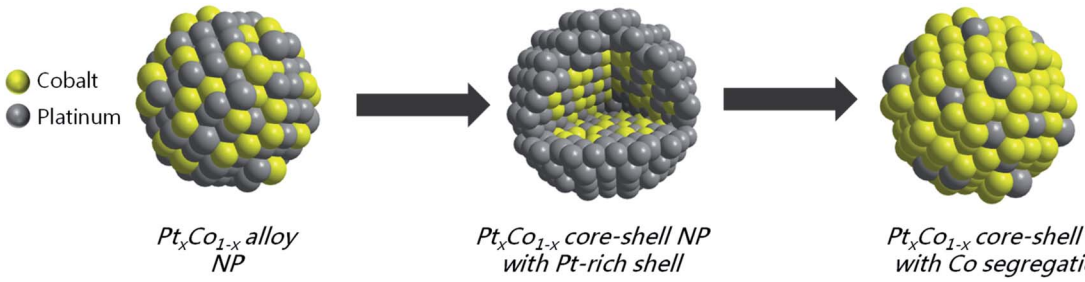

Fig. 2 Illustration of the surface rearrangement of Pt_xCo_{1-x} electrocatalyst along the uniform alloy, Pt-rich shell and Co-segregated core–shell nanoparticle (NP) motifs controlled by the (electro)chemical environment. Pt and Co atoms are symbolized with grey and yellow spheres, respectively.

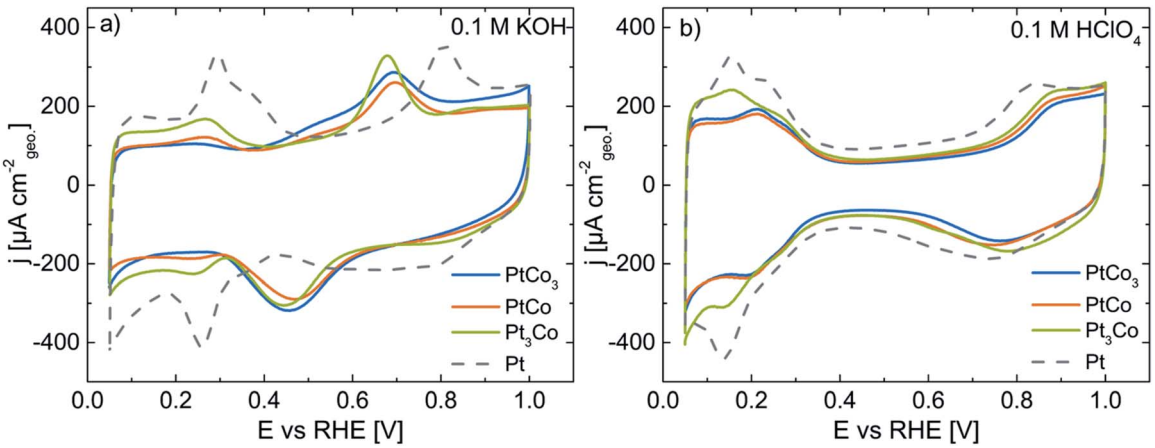

Fig. 3 CV profiles of pristine $PtCo_3$ (blue), PtCo (orange), Pt_3Co (green), and Pt (grey dashed line) in Ar-saturated 0.1 M KOH (a) and after dealloying (0.05–1.00 V *vs.* RHE, 50 mV s^{-1}, and 10 cycles) in Ar-saturated 0.1 M $HClO_4$ (b). All CV profiles were recorded at 50 mV s^{-1} with a Pt loading of 8–10 μg_{Pt} cm_{geo}^{-2}. The current density is normalized to the geometric surface area of the working electrode.

Table 1 Summary of the mean particle size, crystallite size, chemical composition, and metal loading for the as-prepared Pt_xCo_{1-x} catalyst materials and commercially available Pt/HSAC. The values in the bracket denote the results from the Rietveld quantification

Catalyst	Particle size (*via* TEM) [nm]	Crystallite size (*via* XRD) [nm]	Composition (*via* Vergard's law) [at%]	Composition (*via* EDX) [at%]	Pt loading (*via* TGA/EDX) [wt%]
$PtCo_3$	4.4 ± 1.0	3.7 ± 0.1 13.2 ± 0.5	$Pt_{53}Co_{47}$ (61.6 wt%) $Pt_{21}Co_{79}$ (38.4 wt%)	$Pt_{24\pm5}Co_{76\pm5}$	33.1
PtCo	4.2 ± 0.9	2.9 ± 0.1 4.6 ± 0.1	$Pt_{73}Co_{27}$ (69.8 wt%) $Pt_{52}Co_{48}$ (30.2 wt%)	$Pt_{47\pm4}Co_{53\pm4}$	32.0
Pt_3Co	3.8 ± 0.8	4.6 ± 0.1	$Pt_{84}Co_{16}$ (100 wt%)	$Pt_{72\pm5}Co_{28\pm5}$	29.3
Pt	2.6 ± 0.9		Pt_{100}	Pt_{100}	28.4

Table 2 Overview of the changes in ECSA values for Pt_xCo_{1-x} catalysts along the pristine alloy, Pt-rich shell and Co-segregated core–shell nanoparticle motifs in 0.1 M $HClO_4$ and 0.1 M KOH

	$ECSA_{KOH}$, pristine [$m^2\ g_{Pt}^{-1}$]	$ECSA_{HClO_4}$, core–shell [$m^2\ g_{Pt}^{-1}$]	$ECSA_{KOH}$, core–shell [$m^2\ g_{Pt}^{-1}$]	$ECSA_{KOH}$, Co-segr. [$m^2\ g_{Pt}^{-1}$]	particle size *via* TEM [nm]
$PtCo_3$	2 ± 1	41 ± 4	27 ± 3	17 ± 2 4 ± 1[a]	4.4 ± 1.0
PtCo	4 ± 1	44 ± 3	30 ± 3	22 ± 3	4.2 ± 0.9
Pt_3Co	10 ± 2	47 ± 5	37 ± 3	33 ± 3	3.8 ± 0.8
Pt	63 ± 4	77 ± 3			2.6 ± 0.9

[a] Co-segregated $PtCo_3$ core–shell catalyst obtained after 1400 cycles between 0.05 and 1.0 V *vs.* RHE in 0.1 M KOH.

electrochemical features become clearly visible. In Fig. 3a, broad current peaks exist between 0.6–0.7 V and 0.3–0.6 V *vs.* RHE in the anodic and cathodic scans, respectively. According to the Pourbaix diagram, $Co(OH)_2$, CoO, Co_3O_4, and CoOOH are predicted in the investigated potential range at pH 13.[32,33,36] It is noted that for bimetallic systems the reduction/dissolution potential of a metal A surrounded by a more noble metal B might be shifted to more negative potentials compared to its Nernst potential, referred to as underpotential metal deposition.[37,38] Depending on the elemental surface distribution, the shift of the redox potential for Co (hydr)oxide species might be more or less pronounced. We also observed a broadening of these current peaks particularly in the cathodic direction, indicating an overlap of multiple electrochemical reduction processes of active redox species such as $Co_3O_4/Co(OH)_2$, Co_3O_4/CoO and $CoOOH/Co(OH)_2$. Although cobalt oxide materials have intensively been investigated as electrocatalysts for the oxygen evolution reaction (OER) from water under alkaline conditions, the accurate chemical states of Co (hydr)oxide species are dependent on several parameters like pH,[39–42] potential,[39,41–44] pre-treatment,[45] kind of electrolyte,[40,46] *etc.*

Despite a similar particle size and metal loading (see Table 1), the decrease of the current density in the Hupd region with increasing Co content signifies a successive reduction of Pt surface atoms. To quantify this observation, we determined the electrochemically active Pt surface area (ECSA) *via* the Hupd method. In Table 2, the ECSA values are 2 ± 1, 4 ± 1, and 10 ± 2 $m^2\ g_{Pt}^{-1}$ for pristine $PtCo_3$, PtCo, and Pt_3Co in 0.1 M KOH, respectively.

Very remarkably, the CV profiles (Fig. 3a) show the suppression of Pt (hydr)oxide formation between 0.7 and 1.0 V *vs.* RHE with increasing Co content (compared with Pt/HSAC, grey dashed line). The disappearance of Pt (hydr)oxide in the CV profile is also supported by the concurrent decrease of Hupd and the preferred surface enrichment of Co (hydr)oxide species in 0.1 M KOH.

After pre-characterization, the Pt_xCo_{1-x} catalysts were then transferred into Ar-saturated 0.1 M $HClO_4$ and electrochemically treated between 0.05 and 1.00 V *vs.* RHE at 50 mV s^{-1} for 10 cycles by using the cyclic voltammetry (CV) method. This recipe causes a rapid electrochemical dissolution (dealloying) of Co atoms at the surface of alloy nanoparticles due to their negative Nernst potential. Thus, the obtained CV profiles of dealloyed Pt_xCo_{1-x} catalysts resemble the electrochemical features of a clean Pt surface (grey dashed line), as shown in Fig. 3b. We wanted to emphasize that the decay of the Co content within a single particle is not only affected at the top layer, but also in the subsurface layers. Single crystal Pt–M (M = Ni, Co) studies in on ultra-high vacuum have revealed the structural and compositional fluctuations of the first three layers after Co leaching.[47–49] In addition, our previous studies have reported the formation of core–shell nanoparticles with a Pt-rich shell of ~1 nm (3–4 monolayers) and Co-rich particle core induced by dealloying.[30,50] Throughout the paper, the electrochemically dealloyed Pt_xCo_{1-x} nanoparticles will be referred to as core–shell nanoparticles. The enrichment of Pt surface atoms is also confirmed by the strong increase of the ECSA. Irrespective of the initial Co content, the ECSA values are very similar in 0.1 M $HClO_4$ and are determined to be 41 ± 4, 44 ± 3 and 47 ± 5 $m^2\ g_{Pt}^{-1}$ for dealloyed $PtCo_3$, PtCo and Pt_3Co core–shell catalysts, respectively. Although the absolute loss of the Co content for the pristine $PtCo_3$ nanoparticles is

Table 3 Overview of atomic Pt : Co ratios for Pt_xCo_{1-x} catalysts along the pristine alloy, dealloyed, and Co-segregated core–shell nanoparticle motifs obtained from *ex situ* XPS and EDX data. The standard derivations are in the range of 3–5 at%

	Pristine		Core–shell		Co-segregated	
	Pt : Co [at%] EDX	Pt : Co [at%] XPS	Pt : Co [at%] EDX	Pt : Co [at%] XPS	Pt : Co [at%] EDX	Pt : Co [at%] XPS
$PtCo_3$	24 : 76	37 : 63	51 : 49	59 : 41	55 : 45	52 : 48
PtCo	47 : 53	52 : 48	60 : 40	77 : 23	65 : 35	80 : 20
Pt_3Co	72 : 28	75 : 25	78 : 22	91 : 9	81 : 19	89 : 11

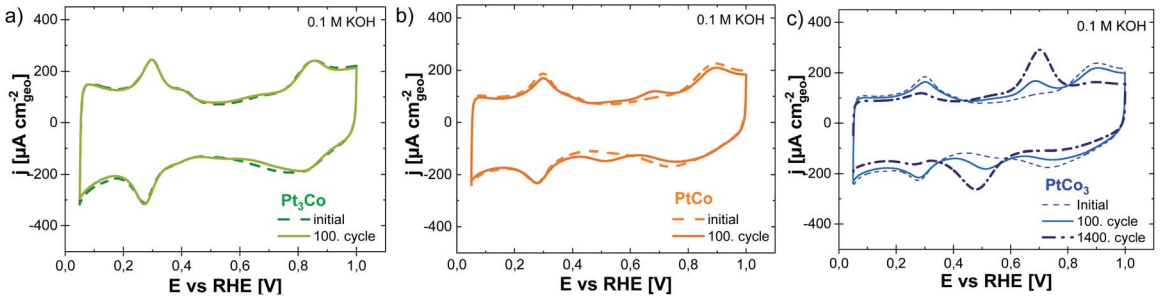

Fig. 4 CV profiles of dealloyed Pt_3Co (a), PtCo (b), and $PtCo_3$ (c) prior to (dashed line) and after (solid line) 100 potential cycles at 50 mV s^{-1} in Ar-saturated 0.1 M KOH. The Co enrichment process mainly reaches a steady-state after potential cycling for up to 1400 scans between 0.05 and 1.0 V *vs.* RHE (dash-point line) in 0.1 M KOH. The current density is normalized to the geometric surface area of the working electrode.

significantly higher than those for the dealloyed PtCo and Pt_3Co (see Table 3), which might result in an increased surface roughness, the ECSA of the dealloyed Pt_xCo_{1-x} electrocatalysts is mainly influenced by the particle size. As large nanoparticles exhibit a lower surface-to-volume ratio compared to small nanoparticles, the highest ECSA value was obtained for pure Pt/HSAC with a particle size of 2.6 ± 0.9 nm.

In the next step, the dealloyed Pt_xCo_{1-x} core–shell nanoparticles were transferred back to a fresh alkaline electrolyte solution. Fig. 4 displays the CV profiles of the dealloyed $PtCo_3$, PtCo, and $PtCo_3$ core–shell catalysts before (dashed line) and after 100 cycles (solid line) in Ar-saturated 0.1 M KOH. First, the initial CV profiles of dealloyed Pt_xCo_{1-x} core–shell nanoparticles (dashed line) resemble the electrochemical characteristics of a pure Pt surface, signifying an enrichment of Pt atoms within the first at least three atomic subsurface layers. After exposure to 0.1 M KOH for 100 cycles, the CV profiles of dealloyed PtCo (Fig. 4b, orange) and $PtCo_3$ (Fig. 4c, blue) have dramatically altered. The re-appearance of broad current peaks between 0.3 and 0.7 V *vs.* RHE is assigned to the Co (hydr)oxide species within the first surface layers (compared with Fig. 3a). Due to their oxophilic character, the Co atoms tend to segregate to the surface induced by increasing OH surface coverage *e.g.* controlled by the potential and pH. This observation evidences that the dealloyed Pt_xCo_{1-x} core–shell nanoparticles can be further altered by modifying their (electro)chemical environment. As the particle size is still unchanged (see Fig. S2 of the ESI†), the gradual surface enrichment of Co atoms is simultaneously accompanied by the decrease of Pt surface atoms. To highlight this atomic re-arrangement, we denoted these modified nanoparticles as Co-segregated core–shell nanoparticles. As the electrochemical Pt features are further visible in the CV profiles, we suggest that both Co and Pt atoms are present at the particle surface. Only the dealloyed Pt_3Co core–shell nanoparticles (Fig. 4a) remained unchanged after applying a similar electrochemical protocol in KOH, which can be explained by the inherently lower Co content compared to the initial PtCo and $PtCo_3$ catalysts, as shown in Tables 1 and 3.

The ECSA determination enables quantifying this adsorbate-induced re-arrangement process of Co and Pt atoms from the initial core–shell towards Co-segregated core–shell nanoparticles. Differences in the initial ECSA values measured in $HClO_4$ and KOH come from the altered enthalpies for hydrogen ad/desorption in the presence of OH^- and H^+.[14,51–53] Therefore, we only compared the ECSA values for dealloyed Pt_xCo_{1-x} catalysts prior to and after 100 potential cycles in 0.1 M KOH. In Table 2, the ECSA values decrease from 27 ± 3 to 17 ± 2 $m^2\ g_{Pt}^{-1}$ (−37%), from 30 ± 3 to 22 ± 3 $m^2\ g_{Pt}^{-1}$ (−26%), and from 37 ± 3 to 33 ± 2 $m^2\ g_{Pt}^{-1}$ (−10%) for the dealloyed $PtCo_3$, PtCo, and Pt_3Co catalysts, respectively. We wanted to stress that this dynamic re-arrangement process of Co and Pt atoms does not lead to a thermodynamically stable state of these bimetallic nanoparticles. Fig. 4c shows the CV profiles of the dealloyed $PtCo_3$ nanoparticles as a course of various potential cycles (1, 100, and 1400) in 0.1 M KOH. The Co (hydr)oxide redox pair get more and more pronounced by additional potential cycling. However, a potential treatment for more than 1400 cycles does not result in an additional growth of the current densities for Co (hydr)oxide species, indicating that a "quasi-stable" state for Co-segregated $PtCo_3$ core–shell nanoparticles has been reached.

This "quasi-stable" CV profile shows still the presence of both Pt and Co atoms in the first surface layers. Very interestingly, a negative potential shift of the hydrogen adsorption (−15 mV) and a strong suppression of Pt (hydr)oxide formation are visible in the CV profile (Fig. 4c). This shift in the Hupd region is very likely caused by the increased coverage of strongly adsorbed OH species (OH_{ad}) on a Co-enriched bimetallic surface and/or changes in the potential of zero charge (pzc) due to its surface re-arrangement.

Advanced X-ray photoelectron spectroscopy (XPS) and energy-dispersive X-ray spectroscopy (EDX) analysis of various surface arrangements of Pt_xCo_{1-x} nanoparticle motifs

Changes in the chemical composition and chemical state of Pt_xCo_{1-x} catalysts along the pristine alloy, dealloyed, and Co-segregated core–shell nanoparticles were probed by *ex situ* XPS and EDX techniques. In Table 3, the EDX data show the highest loss of the Co content for Pt_xCo_{1-x} catalysts after electrochemical dealloying in $HClO_4$. The atomic Pt : Co ratios alter from 24 : 76 to 51 : 49 for $PtCo_3$, from 47 : 53 to 60 : 40 for PtCo, and from 72 : 28 to 78 : 22 for Pt_3Co (standard derivation of 4–5 at%), respectively. The subsequent potential cycling of dealloyed Pt_xCo_{1-x} catalysts in KOH leads to almost unchanged composition, implying their high electrochemical stability in the applied potential range at pH 13. Hence, the surface re-arrangement of bimetallic nanoparticles from dealloyed towards the Co-segregated core–shell structure is not accompanied by electrochemical Co dissolution.

In this work, high-resolution XPS investigations were carried out to establish the chemical state of Co and Pt atoms and their atomic Pt : Co ratio for Pt_xCo_{1-x} catalysts along the structural re-arrangements in detail. Fig. S3† displays the high-resolution XPS spectra of Pt 4f for Pt_xCo_{1-x} catalysts along the pristine alloy (a), dealloyed (c), and Co-segregated (e) core–shell nanoparticle motifs. The Pt 4f XPS spectra were deconvoluted and fitted with double peaks for $4f_{7/2}$ and $4f_{5/2}$, respectively. From the Pt $4f_{7/2}$ peak, three species including metallic Pt^0, Pt^{2+} and Pt^{4+} were identified at binding energies of 71.6, 72.6, and 73.5 eV (reference values[54] of 71.2 ± 0.5 eV, 72.4 ± 0.8, and 74.9 ± 0.8 eV for metallic Pt^0, Pt^{2+} and Pt^{4+}, respectively). In the series of XPS spectra of Pt 4f, no changes in the chemical state of Pt species were observed in this work.

Generally, the XPS analysis of Co 2p is not trivial due to its multiplet spitting, plasmon loss features associated with Co metal[55,56] and shake-up loss features associated with Co oxides.[57] As shown in Fig. 5, the peak broadening is mainly based on the high pass energy of 100 eV (Table S2†) applied due to the very low residual Co content within the thin catalyst films after electrochemical experiments. The Co $2p_{3/2}$ signal was deconvoluted into three peaks at binding energies of *ca.* 778 eV, 781 eV, and 785 eV, which are assigned to metallic Co and oxidized Co species according to the literature.[37,58] It is noted that an unambiguous allocation of various Co (hydr)oxide components, *i.e.* CoO, Co_2O_3, Co_3O_4, CoOOH, $Co(OH)_2$, and $Co(OH)_3$, is very difficult due to their similar binding energies (BE) and shake-up loss features.[55,58–61] Thus, the oxidized Co species are only assigned to Co^{z+} without any accurate chemical state mentioned. The quantification was performed by analyzing the Co $2p_{3/2}$ and Pt $4f_{7/2}$ signals. As it is very difficult to deconvolve plasmon loss features and shake-up loss features from the signal at ~785 eV, only the Co 2p XPS signals at around 778 eV and 781 eV were considered to establish the atomic Co^0 : Co^{z+} ratios in this work.

After synthesis, the XPS data show atomic Pt : Co ratios of 75 : 25, 52 : 48, and 37 : 63 for pristine Pt_3Co, PtCo, and $PtCo_3$, respectively, which is in good agreement with the elemental results obtained from EDX (see Table 3). As expected, the cobalt appears in a metallic and oxidized chemical state within the pristine alloy nanoparticles (Fig. 5). The content of oxidized Co in the as-prepared PtCo and $PtCo_3$ catalysts is more than 50 at%, while the as-prepared Pt_3Co catalyst shows a higher metallic cobalt content (Fig. 5a and b). The appearance of oxidized Co species very likely stems from non-reduced Co precursor salt or/and surface oxide immediately formed upon exposure of metallic cobalt to air. However, no residual $CoNO_3$ precursor was detected from XPS. The XRD profiles (Fig. S1 and Table S1†) show no additional reflexes of Co oxide crystal phases. Based on the XRD and XPS data, we suggest that the observed Co^{z+} species largely exist as amorphous (hydr)oxides. In order to rule out the post-oxidation of Co within the electrochemically treated Pt_xCo_{1-x} catalysts during the sample transfer, a control experiment was performed in an Ar-filled glovebox directly connected to a XPS chamber. Very remarkably, our control experiment in an oxygen-free glovebox reveals that the dealloyed PtCo core–shell catalyst shows a similar amount of Co oxide species (41 at%) compared to that from the RDE experiments (Co^{z+} 45 at%) (not shown, will be published in our next work). Therefore, we suggest that the Pt-enriched surface of dealloyed bimetallic nanoparticles protects the internal Co atoms for post-oxidation of metallic Co in air.

The electrochemical dealloying significantly alters the atomic Co^0 : Co^{z+} ratios of the PtCo and Pt_3Co catalysts. Besides the loss of the total Co content, amorphous Co oxide species at the particle surface rapidly corrode under the harsh conditions (up to 1.0 V *vs.* RHE, pH 1), resulting in an increase of metallic Co species within the dealloyed nanoparticles. However, the dealloyed $PtCo_3$ core–shell catalyst shows an opposite trend, namely an increase of the oxidized Co content. We suggest that the decay of the metallic cobalt content for pristine $PtCo_3$ is very likely attributed to the Co-rich crystal phase detected by XRD (see Fig. S1 and Table S1†). The exchange to alkaline electrochemical conditions does not lead to a significant alteration of Co^0 : Co^{z+} ratios for dealloyed Pt_xCo_{1-x} catalysts. Besides their almost stable chemical composition as discussed above and shown in Table 3, the atomic Co^0 : Co^{z+} ratios for dealloyed Pt_xCo_{1-x} core–shell nanoparticles seem to be not influenced by the Co segregation process. This finding is very surprising because the content of oxidized cobalt species would significantly be increased if internal Co atoms migrate to the top layer and immediately form $Co(OH)_2$ and Co_3O_4 species upon exposure to alkaline electrolyte solution. Actually, we observed a reverse effect that the additional potential cycling up to 1400 to achieve a steady-state CV profile (see Fig. 4c) leads to

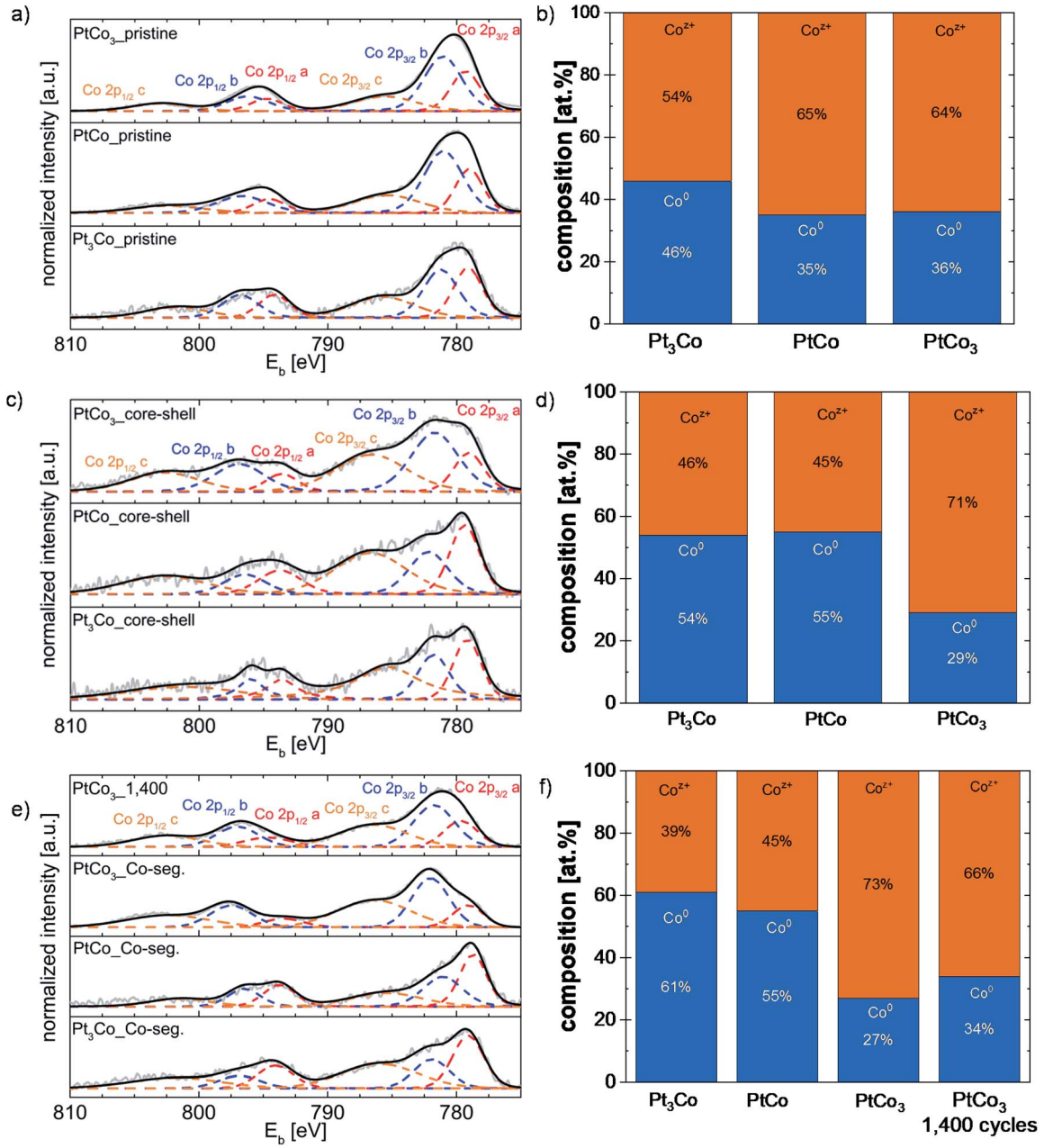

Fig. 5 (a, c and e) High-resolution XPS spectra of Co 2p for Pt_3Co, PtCo, and $PtCo_3$ along the pristine alloy (a), dealloyed (c) and Co-segregated (e) core–shell nanoparticle motifs. Experimental parameters like the step size, pass energy, dwell time and number of scans are listed in Table S2 of the ESI.† The experimental data are denoted as the grey line and the fit is symbolized by the black line. Red, blue and orange dashed lines denote the different Co species. (b, d and f) Bar diagrams display the atomic Co^0 : Co^{z+} ratios of the pristine and treated Pt_xCo_{1-x} catalysts appearing in their various structural nanoparticle motifs.

a transition of oxidized to metallic Co species, Fig. 5e and f. We suggest that this transformation is very likely related to the potential-dependent mobility of surface atoms and its dynamic changes in the coverage of adsorbates. As the surface-sensitive CV profile clearly shows the electrochemical features of redox-active Co (hydr)oxide species in Fig. 4c, we assume that the Co atoms tend to mainly enrich in the subsurface layers of the nanoparticles. But, the most interesting observation is the electrochemical resistance of amorphous Co oxide species within the bimetallic nanoparticles. We suggest that the amorphous Co oxide is a relic from the initial composition of the nanoparticles, which is formed during the fast surface passivation of the remaining noble metal, Pt, under these harsh conditions.

Although metallic Co tends to rapidly dissolve under corrosive conditions, the amorphous Co oxide species appear very stable up to 1.0 V *vs.* RHE at pH 1 (0.1 M $HClO_4$). The high stability of crystalline Co oxide films or Co atoms incorporated in MnO_x or PbO_x crystals as a host substrate at potentials applied for the OER and low pH values (<2.5) has been very recently reported in the

literature.[62–64] An alternative explanation might come from the protecting role of a Pt-enriched particle surface to prevent the electrochemical dissolution of internal Co atoms. Very recently, nanoporous Pt–CoO_x films prepared by a sequential magnetron-sputter process have shown a considerable Pt-based surface area and ORR performance.[65] The origin of the superior ORR activity is based on the lattice strain in the Pt–Pt distance induced by the CoO_x backbone.

In summary, we point out that the nature of the residual Co appears in two chemical states (metallic and oxidized) protected by the Pt-rich shell of dealloyed and Co-segregated Pt_xCo_{1-x} catalysts. The question arises about the role of Co and Pt during the HOR mechanism and how the HOR performance can be tailored by the presence of metallic and oxidized Co.

HOR performance on various surface arrangements of Pt_xCo_{1-x} nanoparticle motifs

The polarization measurements (a, c, and e) for Pt_3Co (green), PtCo (orange), and $PtCo_3$ (blue) catalysts as pristine alloy, dealloyed, and Co-segregated core–shell nanoparticles as well as the corresponding fits (dashed lines; b, d, and f) using the

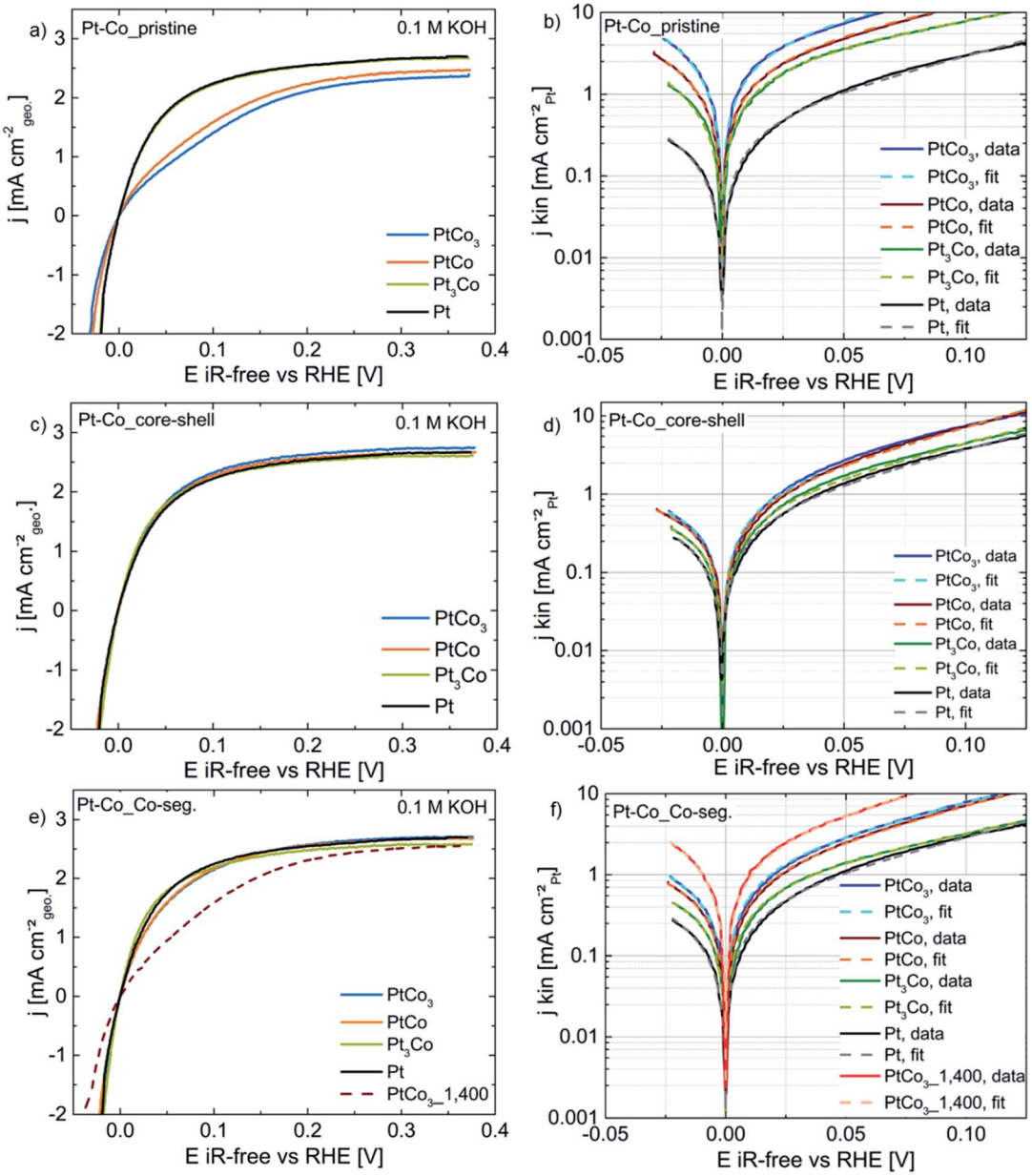

Fig. 6 HOR/HER polarization curves (left) and Butler–Volmer plots (j_{kin} *vs. iR*-corrected *E*, right) of Pt_xCo_{1-x} electrocatalysts in the pristine alloy (a and b), dealloyed Pt-rich shell (c and d) and Co-segregated (e and f) core–shell nanoparticle motifs. The polarization curves were recorded from −0.05 to 0.4 V *vs.* RHE at 1600 rpm and 10 mV s^{-1} in H_2-saturated 0.1 M KOH. The current density is normalized to the geometric surface area of the electrode, while the i_{kin} extracted from the Butler–Volmer equation is normalized by the electrochemically active Pt surface area (ECSA). $PtCo_3$ is coloured in blue, PtCo in orange, Pt_3Co in green and pure Pt in black.

Butler–Volmer equation are shown in Fig. 6. Basically, three different regimes for the HOR polarization curves can be identified: kinetically controlled regime (0.0–0.015 V *vs.* RHE) followed by a mixed regime with contributions of kinetics and mass transport restrictions (0.015–0.15 V), and finally the mass transport-limiting regime (0.15–0.35 V).

First, we will discuss the HOR performance of pristine Pt_xCo_{1-x} alloy catalysts. In Fig. 6a, pristine Pt_3Co and pure Pt show a negative shift of the polarization curves and higher mass transport-limiting current densities compared to pristine PtCo and $PtCo_3$, signifying improved HOR activities due to their Pt-enriched particle surface (large ECSA values, see Table 2 and Fig. 2). Fig. 6b displays a plot of Pt surface area-based kinetic current densities ($j_{kin,spec}$) *vs. iR*-corrected potential to point out the increase of HOR performance in the order of: Pt < Pt_3Co < PtCo < $PtCo_3$, respectively. This opposite trend is very likely attributed to the different ECSA values of pristine Pt_xCo_{1-x} catalysts which will be discussed in detail later.

In Fig. 6c, the HOR polarization curves for dealloyed Pt_xCo_{1-x} core–shell nanoparticles are slightly shifted to negative potentials compared to pure Pt/C. The respective Butler–Volmer plots of $j_{kin,spec}$ *vs. iR*-corrected potential (E) imply a slight activity improvement in the order of: Pt < Pt_3Co < PtCo ≈ $PtCo_3$ prepared by electrochemical dealloying in 0.1 M $HClO_4$.

Fig. 6e displays the HOR/HER polarization curves of Pt_xCo_{1-x} catalysts prepared by a sequence of dealloying in $HClO_4$ and additional 100 potential cycles in 0.1 M KOH. The polarization curves are mainly on top of each other and are similar to those for dealloyed Pt_xCo_{1-x} catalysts. We observed slight differences between these catalysts only in the mixed regime of the HOR polarization curves. More importantly, a direct comparison between Co-segregated $PtCo_3$ core–shell nanoparticles before and after 1400 potential cycles in KOH exhibits a dramatic activity loss. The plots of $j_{kin,spec}$ *vs. iR*-corrected E, yet, imply an opposite trend due to the critical normalization of j_{kin} with a low ECSA value as discussed now.

To benchmark these Pt_xCo_{1-x} catalysts along the pristine alloy, dealloyed, and Co-segregated core–shell nanoparticle motifs for the HOR activity in 0.1 M KOH, we also determined the intrinsic exchange current densities (j^0) and transfer coefficients (α) extracted from the fits using the Butler–Volmer equation. The j^0 values were then normalized with the initial Pt mass (denoted as j^0_{mass}), electrochemically active Pt surface area *via* the Hupd method (j^0_{spec}), and geometric surface area of the working electrode (j^0_{geo}) and are summarized in Tables 4–6.

The j^0_{spec} values were determined to be 4.12 ± 0.42, 2.66 ± 0.17, and 2.02 ± 0.10 mA cm_{Pt}^{-2} for pristine $PtCo_3$, PtCo, and Pt_3Co, respectively. In contrast, the j^0_{mass} increases in the opposite order of: $PtCo_3$ (0.07 ± 0.01 A mg_{Pt}^{-1}) < PtCo (0.12 ± 0.02 A mg_{Pt}^{-1}) < Pt_3Co (0.22 ± 0.04 A mg_{Pt}^{-1}) < pure Pt (0.28 ± 0.02 A mg_{Pt}^{-1}), respectively. The j^0_{geo} shows a similar trend to j^0_{mass}. Although the particle size and loading are nearly the same, this contrary trend between j^0_{spec} and j^0_{mass} (j^0_{geo}) might be caused by the limitation of the accurate ECSA determination particularly if the ECSA value is getting very small (see Table 2 for pristine $PtCo_3$ and PtCo). Alternatively, CO stripping experiments were also applied to establish the ECSA of Pt. However, only the Hupd method has delivered reliable ECSA values for bimetallic Pt–Co surfaces under alkaline conditions, which will be discussed later. On the other hand, j^0_{mass} and j^0_{geo} dramatically decrease with increasing Co content for the pristine alloys, while the catalytic HOR performance of pristine Pt_3Co is nearly comparable with that of pure Pt within the error range. Very importantly, the transfer coefficients (α) for all pristine Pt_xCo_{1-x} catalysts are below 0.5, signifying an asymmetric behaviour between the HOR and HER branches and thus modification in reaction pathways on a Co-rich bimetallic surface. As the intrinsic catalytic reactivity of pure Co is very low, we can conclude that the preferred formation of OH_{ad} on a Co-rich Pt–Co surface dramatically alters the activity and reaction pathways for the HOR in alkaline media.

Table 4 HOR exchange current densities normalized by the Pt surface area specific (j^0_{spec}), Pt mass used (j^0_{mass}), and geometric surface area of the electrode (j^0_{geo}) as well as transfer coefficients (α) of pristine Pt_xCo_{1-x} catalysts in H_2-saturated 0.1 M KOH

Pristine Pt_xCo_{1-x}	j^0_{spec} [mA cm_{Pt}^{-2}]	j^0_{mass} [A mg_{Pt}^{-1}]	j^0_{geo} [mA cm_{geo}^{-2}]	α [a.u.]
$PtCo_3$	4.12 ± 0.42	0.07 ± 0.01	0.66 ± 0.07	0.38 ± 0.05
PtCo	2.66 ± 0.17	0.12 ± 0.02	1.00 ± 0.07	0.39 ± 0.05
Pt_3Co	2.02 ± 0.10	0.22 ± 0.04	2.10 ± 0.12	0.35 ± 0.03
Pt	0.55 ± 0.03	0.28 ± 0.02	2.40 ± 0.38	0.50 ± 0.02

Table 5 HOR exchange current densities normalized by the Pt surface area specific (j^0_{spec}), Pt mass used (j^0_{mass}), and geometric surface area of the electrode (j^0_{geo}) as well as transfer coefficients (α) of dealloyed Pt_xCo_{1-x} core–shell catalysts in H_2-saturated 0.1 M KOH

Dealloyed Pt_xCo_{1-x} core–shell	j^0_{spec} [mA cm_{Pt}^{-2}]	j^0_{mass} [A mg_{Pt}^{-1}]	j^0_{geo} [mA cm_{geo}^{-2}]	α [a.u.]
$PtCo_3$	1.04 ± 0.08	0.24 ± 0.02	2.28 ± 0.15	0.53 ± 0.02
PtCo	0.94 ± 0.09	0.25 ± 0.01	2.38 ± 0.25	0.50 ± 0.03
Pt_3Co	0.67 ± 0.06	0.26 ± 0.03	2.18 ± 0.28	0.52 ± 0.02
Pt	0.55 ± 0.03	0.28 ± 0.02	2.40 ± 0.38	0.50 ± 0.02

Very interestingly, the dealloyed Pt_xCo_{1-x} catalysts with a Pt-rich particle shell exhibit similar HOR activities with respect to j^0_{mass} and j^0_{geo} and are comparable to pure Pt/HSAC, as listed in Table 5. Only the j^0_{spec} values increase in the order of: Pt(0.55 ± 0.03 mA cm_{Pt}^{-2}) < Pt_3Co(0.67 ± 0.06 mA cm_{Pt}^{-2}) < PtCo(0.94 ± 0.09 mA cm_{Pt}^{-2}) < $PtCo_3$(1.04 ± 0.08 mA cm_{Pt}^{-2}), respectively. Thus, the j^0_{spec} values for the dealloyed PtCo and $PtCo_3$ core–shell catalysts improve by a factor of 1.5–1.9 compared to pure Pt/HSAC and dealloyed Pt_3Co. Very recently, we have shown no influence of the particle size of polycrystalline and nano-sized Pt on the HOR activity in alkaline media.[13,27] Thus, the improved j^0_{spec} for dealloyed PtCo and $PtCo_3$ core–shell nanoparticles is very likely caused by the geometric effect in the Pt-enriched shell surrounded by the Pt–Co-CoO_x particle core, lowering the Pt–H binding energy. Other research groups have recently reported an improved HOR activity on a strained Pt surface (reduced Pt–Pt distance) for Pt–Ni and Pt–Ru systems due to the modified hydrogen binding energy.[7,9,10] Changes in Pt–H binding energy is often related to the potential shift of the hydrogen desorption in the Hupd region. As shown in Fig. S4,† a potential shift of the H desorption is not observed for all dealloyed Pt_xCo_{1-x} core–shell nanoparticles irrespective of the initial Co content and possible characteristics in the formed Pt-enriched particle shell *e.g.* differences in the shell thickness and composition of the particle core. Only the reduction of the Pt (hydr)oxide current peak is significantly shifted to more negative potentials compared to that for pure Pt and dealloyed Pt_3Co, implying a decrease of OH_{ad} coverage and thus an improved ORR performance. In fact, the compressive strain in the Pt shell only results in the improvement of j^0_{spec}, but the magnitude of HOR activity enhancement is much less pronounced compared to that for the ORR. The transfer coefficients (α) for all dealloyed Pt_xCo_{1-x} core–shell catalysts were determined to be around 0.5, which is in very good agreement with that for pure Pt. The resulting symmetry for the HER and HOR branches implies similar reaction pathways on dealloyed core–shell catalysts with a Pt-rich shell.

After 100 potential cycles in 0.1 M KOH, the influence of the re-appearance of Co atoms in the subsurface layers on the catalytic HOR performance is displayed in Fig. 6 and Table 6. Compared to the dealloyed catalysts with a Pt-rich particle shell (Fig. 6c, d and Table 5), the values of j^0_{mass} and j^0_{geo} for the Co-segregated PCo and $PtCo_3$ core–shell nanoparticles are almost unchanged and are thus similar to those of pure Pt. However, the j^0_{spec} increases up to 2.6 particularly for the Co-segregated $PtCo_3$ core–shell nanoparticles compared to pure Pt. To correlate the increase of j^0_{spec} with the Co segregation, it is necessary to compare dealloyed $PtCo_3$ with dealloyed Pt_3Co. First, the re-appearance of Co (hydr)oxide species is not observed for dealloyed Pt_3Co after 100 potential cycles in 0.1 M KOH due to the inherently low Co content within the dealloyed nanoparticles. In this case, the improved j^0_{spec} for dealloyed Pt_3Co core–shell nanoparticles is very likely related to the drop of the ECSA (from 37 ± 3 to 33 ± 3 m^2 g_{Pt}^{-1}, −11%, Table 2) due to the carbon corrosion associated with particle detachment as the main degradation process in strong alkaline media.[66,67] In the other case, the j^0_{mass} and j^0_{geo} for the Co-segregated $PtCo_3$ core–shell nanoparticles decrease with gradual enrichment of Co surface atoms induced by additional potential cycles. Thus, the increase of j^0_{spec} might be caused by the discrepancy to determine the accurate ECSA of Pt in the presence of stable Co atoms in the sub-surface layers. To the best of the authors' knowledge, the Hupd method seems to be the reliable and reproducible approach for ECSA determination of Pt surrounded by oxidized Co species under alkaline conditions. Similar trends for the HER performance are observed in this work (see Fig. S5†). Apart from the drastic activity drop, the transfer coefficient decreases from 0.47 ± 0.01 to 0.38 ± 0.02 with successive Co enrichment at the particle surface and reached values similar to those of pristine Pt_xCo_{1-x} alloy catalysts.

Correlation between the HOR activities and Q(Hupd)/Q(Co^{z+}) ratio

To evaluate the elemental distribution within the first surface layers and thus to point out the role of cobalt as an oxophilic component for the catalytic HOR performance, we developed a new descriptor by relating the electric charges yielded from the hydrogen ad/desorption and Co(hydr)oxide reduction/formation, the so-called Q(Hupd)/Q(Co^{z+}) ratio (see Fig. S6†). According to the Pourbaix diagram, $Co(OH)_2$, CoO, Co_3O_4, and CoOOH are predicted in the investigated potential range at pH 13.[32,33] The respective redox potentials and the extended Pourbaix diagram of the cobalt–water system are given in Fig. S7 of the ESI.† It is noted that the redox pair of Co_3O_4/$Co(OH)_2$ and CoOOH/$Co(OH)_2$ are controversially discussed in the literature, which might be based on the pre-treatment,[45] electrochemical conditions[36,39–42,68] and nature[44,69] of Co oxide-based materials as well as the discrimination of different meta-stable Co(hydr)

Table 6 HOR exchange current densities normalized by the Pt surface area specific (j^0_{spec}), Pt mass used (j^0_{mass}), and geometric surface area of the electrode (j^0_{geo}) as well as transfer coefficients (α) of Co-segregated Pt_xCo_{1-x} core–shell catalysts in H_2-saturated 0.1 M KOH

Co-segregated Pt_xCo_{1-x} core–shell	j^0_{spec} [mA cm_{Pt}^{-2}]	j^0_{mass} [A mg_{Pt}^{-1}]	j^0_{geo} [mA cm_{geo}^{-2}]	α [a.u.]
$PtCo_3$	1.43 ± 0.05	0.24 ± 0.02	2.10 ± 0.15	0.47 ± 0.01
$PtCo_3$_1400[a]	2.61 ± 0.2	0.09 ± 0.01	0.80 ± 0.14	0.38 ± 0.02
PtCo	1.09 ± 0.09	0.22 ± 0.03	2.10 ± 0.33	0.46 ± 0.01
Pt_3Co	0.80 ± 0.07	0.29 ± 0.03	2.40 ± 0.37	0.47 ± 0.01
Pt	0.55 ± 0.03	0.28 ± 0.02	2.40 ± 0.40	0.50 ± 0.02

[a] Co-segregated $PtCo_3$ core–shell catalyst obtained after 1400 cycles between 0.05 and 1.0 V *vs.* RHE in 0.1 M KOH.

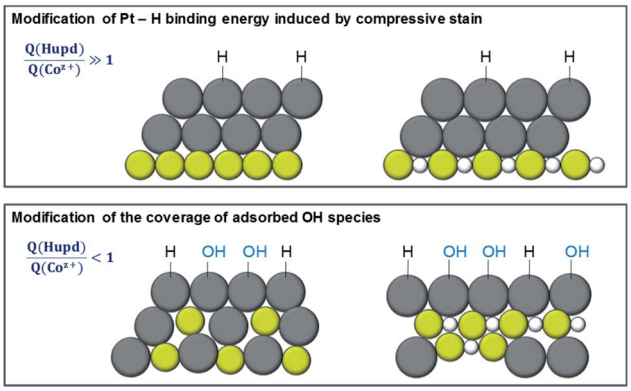

Fig. 7 Illustration of the different surface arrangements of platinum and cobalt in a metallic or oxidized state to tailor the HOR performance in an alkaline environment. Top panel: Metal–H bond mechanism to lower/strengthen the bond of adsorbed hydrogen on a strained Pt top layer surrounded by metallic Co (left) or CoO (right) underlay. Bottom panel: Bifunctional mechanism, where the coverage of OH_{ad} species is attributed to the enrichment of Co and Co oxide species near the surface. The here developed new descriptor, Q(Hupd)/$Q(Co^{z+})$ ratio, expresses the elemental distribution of Co and Pt in the first surface layers. Grey, yellow and white balls denote Pt, Co and O, respectively.

oxide species[40,41,44,46] on the electrode surface. According to the Pourbaix diagram[32,33] and other research studies,[41,43,46,63,68,70] we consider the redox pair of $Co_3O_4/Co(OH)_2$ with the following electrochemical reaction: $3Co(OH)_2 + 2OH^- \rightarrow Co_3O_4 + 4H_2O + 2e^-$. If the value of the Q(Hupd)/$Q(Co^{z+})$ ratio is larger than or below one, the particle surface consists of an excess of Pt or Co to accelerate or block the kinetics of the HOR by forming OH_{ad} species. To illustrate the modification of HOR performance by Pt–H binding energy and coverage of OH_{ad}, Fig. 7 shows a sketch of the 2D atomic arrangement of Pt and Co within the nanoparticles. Due to the chemical properties of Co, this bimetallic catalyst system with different atomic arrangements enables discriminating between the Pt–H_{ad} binding energy model and bifunctional model. The coverage of OH_{ad} species can be modified on these different particle motifs (disordered alloy *vs.* Co-segregated core–shell) and different Co surface contents. In other words, the concentration of Co surface atoms strongly correlates with the coverage of OH_{ad} species which play a critical role in the bifunctional mechanism for the HOR in alkaline media.

It is noted that the enhanced oxophilic character of the Co-segregated $PtCo_3$ core–shell catalyst compared to a Pt-enriched shell is also evident from CO oxidation. Fig. S8† displays the CO stripping experiments of Pt-enriched and Co-segregated core–shell catalysts, signifying a broad oxidation peak at ~0.43 V *vs.* RHE. The second CV profile signifies an irreversible process due to its disappearance. Based on the CO stripping experiments, we also tried to establish the ECSA of Pt. By integrating the charge of the oxidation of the adsorbed CO monolayer from 0.38 and 0.79 V *vs.* RHE, the ECSA value became extremely large for Co-segregated core–shell nanoparticles. This observation cannot be explained by the changes in the particle size (same volume-to-surface ratio) and leads to an overestimation of the ECSA of Pt.

In Table 7, the values of Q(Hupd)/$Q(Co^{z+})$ ratios for as-prepared Pt_xCo_{1-x} increases in the order of: $PtCo_3$ (0.14 ± 0.03) < PtCo (0.25 ± 0.02) < Pt_3Co (1.21 ± 0.07), respectively. This trend shows a successive enrichment of Pt surface atoms with decreasing Co content. On the other hand, the values of Q(Hupd)/$Q(Co^{z+})$ ratios were determined to be 6.4 ± 0.8 and 20.0 ± 2.0 for the Co-segregated $PtCo_3$ and PtCo core–shell catalysts. In fact, the pristine PtCo and $PtCo_3$ catalysts indicate a higher contribution of Co surface atoms compared to the Co-segregated PtCo and $PtCo_3$ core–shell nanoparticles. We wanted to emphasize that the observed changes in the value of Q(Hupd)/$Q(Co^{z+})$ ratios are very likely related to the modification of the chemical surface composition and re-arrangement of the bimetallic nanoparticles instead of changes in the particle size (compare Fig. 1 with Fig. S2†). Almost no changes in electrochemical features for dealloyed Pt_3Co were observed after 100 potential cycles in KOH (see Fig. 4a), which might be explained by the inherently low Co content after dealloying in $HClO_4$.

Fig. 8 shows the relationship between the obtained Pt surface area-based specific (j^0_{spec}, panel a), Pt mass-based (j^0_{mass}, panel b) and geometric-normalized (j^0_{geo}, panel c) HOR exchange current densities as a function of the Q(Hupd)/$Q(Co^{z+})$ ratio for pristine Pt_xCo_{1-x} and Co-segregated PtCo and $PtCo_3$ core–shell catalysts. The dashed lines in Fig. 8 denote the respective activities of pure Pt/HSAC and dealloyed $PtCo_3$ core–shell catalysts with a Pt-rich particle shell. As mentioned above and shown in Fig. 7, the lattice strain in the Pt-enriched shell has less influence in weakening the Pt–H bond. The induced strain in the Pt-rich shell is originated from the sublayers consisting of Co and Co oxide species, resulting in a moderate weakening of the Pt–H bond. On the other hand, the Pt-rich top layer protects the further dissolution of internal Co and Co oxide species in the sub-layers. A detailed study for obtaining information about the arrangement and distribution of metallic and oxidized cobalt atoms is currently in progress. Due to the moderate modification of the Pt–H bond induced by the compressive strain in the Pt-rich shell, we focus now on the bifunctional mechanism, in which reactive OH_{ad} might promote the oxidation of H_{ad} on Pt sites according to the Volmer step ($M–H_{ad} + OH^- \rightarrow M + H_2O + e^-$).

Table 7 Q(Hupd)/$Q(Co^{z+})$ ratio values as a descriptor for pristine and Co-segregated Pt_xCo_{1-x} nanoparticles in 0.1 M KOH by integration of the electric charges yielded from the hydrogen ad/desorption and redox reaction of $Co_3O_4/Co(OH)_2$

	Q(Hupd)/$Q(Co^{z+})$	Q(Hupd)/$Q(Co^{z+})$
Pt_xCo_{1-x}	Pristine	Co-segregated
$PtCo_3$	0.14 ± 0.03	6.4 ± 0.8
$PtCo_3$_1400[a]		0.3 ± 0.1
PtCo	0.25 ± 0.02	20.0 ± 2.0
Pt_3Co	1.21 ± 0.07	—

[a] Co-segregated $PtCo_3$ core–shell catalyst obtained after 1400 cycles between 0.05 and 1.0 V *vs.* RHE in 0.1 M KOH.

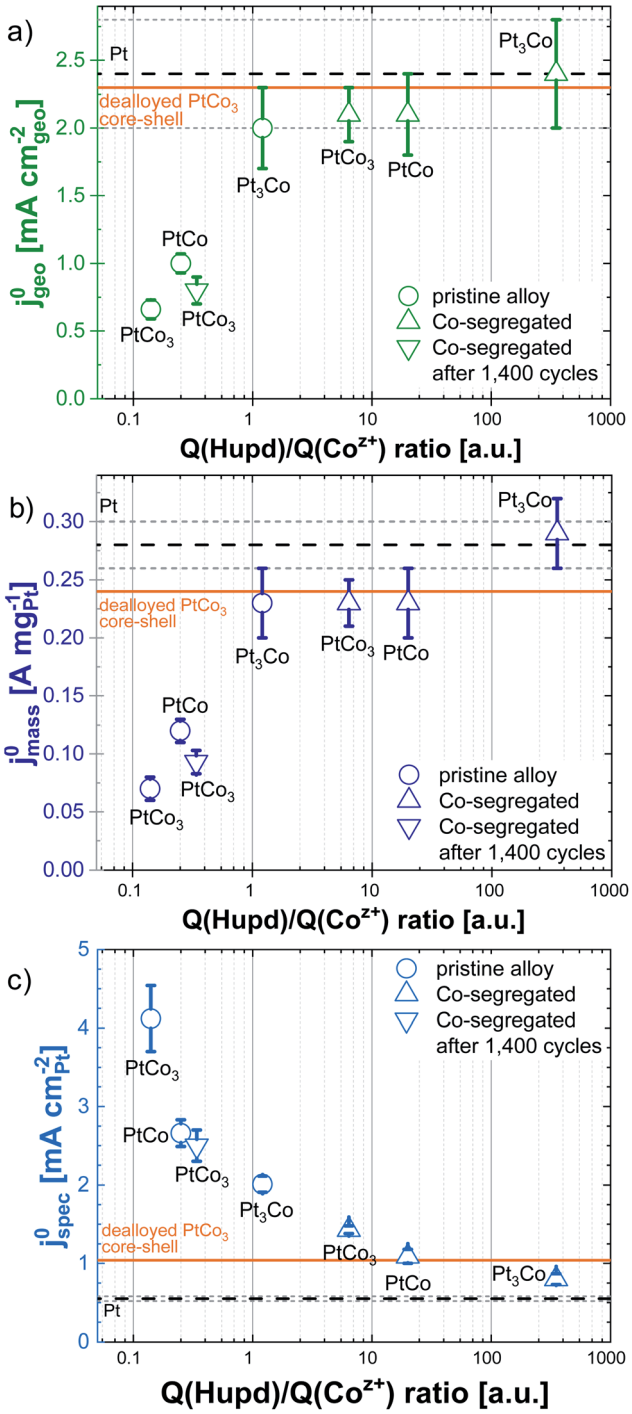

Fig. 8 Relationship between the geometric-normalized (j^0_{geo}, panel a), Pt mass-based (j^0_{mass}, panel b) and Pt surface area-based specific (j^0_{spec}, panel c) HOR exchange current densities as a function of the Q(Hupd)/Q(Co^{z+}) ratio for pristine Pt_xCo_{1-x} and Co-segregated PtCo and $PtCo_3$ core–shell catalysts. The pristine alloy catalysts are denoted with a hollow circle (○), while the Co-segregated core–shell catalysts are symbolized with a hollow triangle (Δ). The Co-segregated $PtCo_3$ core–shell catalyst after 1400 potential cycles is denoted by a hollow inverted triangle. Even though no segregation of Co was observed, we decided to include the dealloyed Pt_3Co core–shell catalyst as a reference in these plots. Pure Pt/HSAC (black dashed lines) and dealloyed $PtCo_3$ core–shell catalysts (orange solid line) with a Pt-rich shell were also taken as reference materials. The grey dashed lines denote the standard deviation of the HOR activity of pure Pt/HSAC.

First, we will discuss the correlation between the HOR performance and Q(Hupd)/Q(Co^{z+}) ratio for pristine Pt_xCo_{1-x} alloy catalysts. In Fig. 8a, the j^0_{spec} increases with increasing initial Co content, when j^0 is normalized by the number of catalytically active Pt sites. This suggests that the nearby oxophilic Co atoms accelerate the kinetics of the HOR on the Pt surface based on the bifunctional mechanism. However, in Fig. 8b and c a reverse effect is observed for j^0_{mass} and j^0_{geo},- namely that the increased appearance of Co surface atoms reduces dramatically the kinetics of the HOR by blocking the surface with strongly OH_{ad} species. Only the pristine Pt_3Co catalyst with a value of the Q(Hupd)/Q(Co^{z+}) ratio which is larger than one shows similar j^0_{mass} and j^0_{geo} to pure Pt/HSAC and dealloyed $PtCo_3$ core–shell catalysts.

The Co-segregated PtCo core–shell catalyst shows an order of magnitude higher value of the Q(Hupd)/Q(Co^{z+}) ratio compared to the Co-segregated $PtCo_3$ catalyst, but both values are significantly larger than one, indicating a large number of available Pt surface atoms. We suggest that this difference also reflects the coverage of OH_{ad} species at the particle surface and is therefore much lower than those for pristine alloys. In a broader sense, the Co-segregated core–shell nanoparticles simulate a Pt-enriched surface with "isolated less noble metal (hydr)oxide clusters". With this picture in mind and illustrated in Fig. 7, our results reveal that a variation of OH_{ad} species for the Pt–Co system does not cause an enhancement of HOR activity in an alkaline environment. Unlike, the comparison of the dealloyed $PtCo_3$ core–shell catalyst after 100 and 1400 potential cycles shows a dramatic decrease of j^0_{mass} and j^0_{geo} due to the additional enrichment of Co atoms within the first surface layers.

Based on our new descriptor, a broad range of Co-containing bimetallic surfaces were investigated in this work. Actually, it was expected that different Co-containing particle surfaces allow tailoring the coverage of OH_{ad} species to facilitate the oxidation of H_{ad} at low potentials (bottom panel of Fig. 8). This approach very likely mimics a single Pt(111) crystal surface decorated with Ni (hydr)oxide clusters to generate reactive OH_{ad} species for the HOR reported by Markovic and coworkers.[23] This so-called bifunctional mechanism to enhance the HOR reactivity is not observed for pristine Pt_xCo_{1-x} alloy and Co-segregated PtCo and $PtCo_3$ core–shell catalysts. In this work, a reserve effect is highlighted, when the Co surface content increases in Pt-based nanoparticles. These findings are very likely related to the formation of "unreactive" OH_{ad} species in the Hupd region, which strongly block the catalytically active Pt sites for the oxidation of H_{ad}. The blockage of catalytically active Pt sites with oxophilic Co neighboring atoms is associated with the suppression of formation/reduction of Pt (hydr)oxide species, as shown in Fig. 4. Altogether, cobalt as an oxophilic component strongly binds the OH_{ad} species, resulting in a lowering of the HOR activity on the Pt-based surface in an alkaline environment.

Conclusions

In this work, we presented a comprehensive study about Pt_xCo_{1-x} catalysts along the uniform alloy, Pt-rich shell, and Co-segregated

core–shell nanoparticle motifs towards enhancing HOR performance in alkaline media. The atomic re-arrangement within the bimetallic nanoparticles can be controlled by the (electro)chemical environment like potential and pH. The oxophilic cobalt is used to tailor the coverage of OH_{ad} species, which play a critical role in the bifunctional mechanism. But on the other hand, the alloying of Pt with Co modifies the electronic and geometric structure of the Pt-enriched shell, which might weaken or strengthen the Pt–H bond. Very remarkably, the XPS analysis signifies not only a metallic but also an amorphous Co oxide species inside the dealloyed and Co-segregated Pt_xCo_{1-x} core–shell catalysts. We assume that the amorphous Co oxide stemmed from the synthesis and air-storage is protected by the Pt-enriched shell under these harsh conditions. Depending on whether metallic or amorphous Co oxide species, the induced lattice strain in the Pt-enriched shell causes only a moderate lowering of the Pt–H binding energy, resulting in an increase of the Pt surface area specific exchange current density j^0_{spec} by a factor of $\sim$2 compared to pure Pt. Our second approach to control the coverage of OH_{ad} species is realized by comparing different Co surface concentrations (pristine alloys *vs.* Co-segregated). Tailoring the coverage of OH_{ad} species enables promoting the oxidation of H_{ad} on the Pt sites, referred to as a bifunctional mechanism. In this context, we developed a new descriptor, namely the $Q(\mathrm{Hupd})/Q(Co^{z+})$ ratio, to evaluate the atomic distribution of Co and Pt at the particle surface.

Our results indicate that the cobalt strongly adsorbs OH_{ad} species at low potentials and thus block the catalytically active Pt sites for the HOR in alkaline media. The blockage of catalytically active Pt sites with strongly oxophilic Co neighboring atoms is associated with the suppression of formation/reduction of Pt (hydr)oxide species. It is noted, that there is still a lack of methods to determine the real electrochemically active Pt surface area on bimetallic surfaces consisting of Pt and Co atoms.

Despite the separation of these critical parameters, cobalt as an oxophilic component strongly bonds OH_{ad} species at the particle surface and the induced lattice strain in the Pt-enriched shell causes only a moderate lowering of the Pt–H binding energy to enhance the kinetics of the HOR in an alkaline environment.

Conflicts of interest

There are no conflicts to declare.

Acknowledgements

DJW and MO are gratefully acknowledged the Bundesministerium für Bildung und Forschung (BMBF, FKZ 03SF0539) for financial support. Furthermore, we thank the DFG for funding the JEOL JEM2100F TEM (INST 184/106-1 FUGG), ESCALAB 250 Xi XPS spectrometer (INST 184/144-1 FUGG), and Empyrean Theta-Theta diffractometer Panalytical (INST 184/154-1 FUGG).

References

1 J. Moorhouse, *Modern Chlor-Alkali Technology*, Wiley, 2007.
2 K. Zeng and D. Zhang, Recent progress in alkaline water electrolysis for hydrogen production and applications, *Prog. Energy Combust. Sci.*, 2010, **36**, 307–326.
3 S. S. Djokic, *Electrodeposition – Theory and Practice*, Springer-Verlag, New York, 2010, ch. XVII, vol. 48, p. 295.
4 R. W. Revie, *Uhlig's Corrosion Handbook*, 2011, pp. i–xxvii.
5 H. A. Gasteiger, S. S. Kocha, B. Sompalli and F. T. Wagner, Activity benchmarks and requirements for Pt, Pt-alloy, and non-Pt oxygen reduction catalysts for PEMFCs, *Appl. Catal., B*, 2005, **56**, 9–35.
6 J. Durst, A. Siebel, C. Simon, F. Hasche, J. Herranz and H. A. Gasteiger, New insights into the electrochemical hydrogen oxidation and evolution reaction mechanism, *Energy Environ. Sci.*, 2014, **7**, 2255–2260.
7 J. N. Schwämmlein, B. M. Stühmeier, K. Wagenbauer, H. Dietz, V. Tileli, H. A. Gasteiger and H. A. El-Sayed, Origin of Superior HOR/HER Activity of Bimetallic Pt–Ru Catalysts in Alkaline Media Identified *via* Ru@Pt Core-Shell Nanoparticles, *J. Electrochem. Soc.*, 2018, **165**, H229–H239.
8 Y. Wang, G. Wang, G. Li, B. Huang, J. Pan, Q. Liu, J. Han, L. Xiao, J. Lu and L. Zhuang, Pt–Ru catalyzed hydrogen oxidation in alkaline media: oxophilic effect or electronic effect?, *Energy Environ. Sci.*, 2015, **8**, 177–181.
9 S. Lu and Z. Zhuang, Investigating the Influences of the Adsorbed Species on Catalytic Activity for Hydrogen Oxidation Reaction in Alkaline Electrolyte, *J. Am. Chem. Soc.*, 2017, **139**, 5156–5163.
10 K. Elbert, J. Hu, Z. Ma, Y. Zhang, G. Chen, W. An, P. Liu, H. S. Isaacs, R. R. Adzic and J. X. Wang, Elucidating Hydrogen Oxidation/Evolution Kinetics in Base and Acid by Enhanced Activities at the Optimized Pt Shell Thickness on the Ru Core, *ACS Catal.*, 2015, **5**, 6764–6772.
11 J. Li, S. Ghoshal, M. K. Bates, T. E. Miller, V. Davies, E. Stavitski, K. Attenkofer, S. Mukerjee, Z.-F. Ma and Q. Jia, Experimental Proof of the Bifunctional Mechanism for the Hydrogen Oxidation in Alkaline Media, *Angew. Chem., Int. Ed. Engl.*, 2017, **56**, 15594–15598.
12 R. Subbaraman, D. Tripkovic, K.-C. Chang, D. Strmcnik, A. P. Paulikas, P. Hirunsit, M. Chan, J. Greeley, V. Stamenkovic and N. M. Markovic, Trends in activity for the water electrolyser reactions on 3d M(Ni,Co,Fe,Mn) hydr(oxy)oxide catalysts, *Nat. Mater.*, 2012, **11**, 550–557.
13 W. Sheng, H. A. Gasteiger and Y. Shao-Horn, Hydrogen Oxidation and Evolution Reaction Kinetics on Platinum: Acid *vs*. Alkaline Electrolytes, *J. Electrochem. Soc.*, 2010, **157**, B1529–B1536.
14 W. Sheng, Z. Zhuang, M. Gao, J. Zheng, J. G. Chen and Y. Yan, Correlating hydrogen oxidation and evolution activity on platinum at different pH with measured hydrogen binding energy, *Nat. Commun.*, 2015, **6**, 5848.
15 J. Durst, C. Simon, A. Siebel, P. J. Rheinländer, T. Schuler, M. Hanzlik, J. Herranz, F. Hasché and H. A. Gasteiger, (Invited) Hydrogen Oxidation and Evolution Reaction (HOR/HER) on Pt Electrodes in Acid *vs.* Alkaline Electrolytes: Mechanism, Activity and Particle Size Effects, *ECS Trans.*, 2014, **64**, 1069–1080.

16 A. B. Anderson, R. A. Sidik, J. Narayanasamy and P. Shiller, Theoretical Calculation of Activation Energies for Pt + H + (aq) + e - (U) ↔ Pt–H: Activation Energy-Based Symmetry Factors in the Marcus Normal and Inverted Regions, *J. Phys. Chem. B*, 2003, **107**, 4618–4623.

17 Y. Cai and A. B. Anderson, The Reversible Hydrogen Electrode: Potential-Dependent Activation Energies over Platinum from Quantum Theory, *J. Phys. Chem. B*, 2004, **108**, 9829–9833.

18 T. Zhang and A. B. Anderson, Hydrogen Oxidation and Evolution on Platinum Electrodes in Base: Theoretical Study, *J. Phys. Chem. C*, 2007, **111**, 8644–8648.

19 J. K. Nørskov, T. Bligaard, A. Logadottir, S. Bahn, L. B. Hansen, M. Bollinger, H. Bengaard, B. Hammer, Z. Sljivancanin, M. Mavrikakis, Y. Xu, S. Dahl and C. J. H. Jacobsen, Universality in Heterogeneous Catalysis, *J. Catal.*, 2002, **209**, 275–278.

20 I. Ledezma-Yanez, W. D. Z. Wallace, P. Sebastián-Pascual, V. Climent, J. M. Feliu and M. T. M. Koper, Interfacial water reorganization as a pH-dependent descriptor of the hydrogen evolution rate on platinum electrodes, *Nat. Energy*, 2017, **2**, 972.

21 R. Rizo, E. Sitta, E. Herrero, V. Climent and J. M. Feliu, Towards the understanding of the interfacial pH scale at Pt(1 1 1) electrodes, *Electrochim. Acta*, 2015, **162**, 138–145.

22 D. Strmcnik, M. Uchimura, C. Wang, R. Subbaraman, N. Danilovic, D. van der Vliet, A. P. Paulikas, V. R. Stamenkovic and N. M. Markovic, Improving the hydrogen oxidation reaction rate by promotion of hydroxyl adsorption, *Nat. Chem.*, 2013, **5**, 300–306.

23 R. Subbaraman, N. Danilovic, D. Strmcnik, K.-C. Chang, A. P. Paulikas, V. R. Stamenkovic and N. M. Markovic, Enhancing the Alkaline Hydrogen Evolution Reaction Activity through the Bifunctionality of Ni(OH) 2/Metal Catalysts, *Angew. Chem.*, 2012, **124**, 12663–12666.

24 D. Strmcnik, P. P. Lopes, B. Genorio, V. R. Stamenkovic and N. M. Markovic, Design principles for hydrogen evolution reaction catalyst materials, *Nano Energy*, 2016, **29**, 29–36.

25 R. Subbaraman, D. Tripkovic, D. Strmcnik, K.-C. Chang, M. Uchimura, A. P. Paulikas, V. Stamenkovic and N. M. Markovic, Enhancing Hydrogen Evolution Activity in Water Splitting by Tailoring Li^+-$Ni(OH)_2$-Pt Interfaces, *Science*, 2011, **334**, 1256–1260.

26 Y. Cong, B. Yi and Y. Song, Hydrogen oxidation reaction in alkaline media: From mechanism to recent electrocatalysts, *Nano Energy*, 2018, **44**, 288–303.

27 D. J. Weber, M. Janssen and M. Oezaslan, Effect of Monovalent Cations on the HOR/HER Activity for Pt in Alkaline Environment, *J. Electrochem. Soc.*, 2019, **166**, F66–F73.

28 M. Oezaslan, F. Hasché and P. Strasser, Oxygen Electroreduction on $PtCo_3$, PtCo and Pt_3Co Alloy Nanoparticles for Alkaline and Acidic PEM Fuel Cells, *J. Electrochem. Soc.*, 2012, **159**, B394.

29 M. Oezaslan and P. Strasser, Activity of dealloyed $PtCo_3$ and $PtCu_3$ nanoparticle electrocatalyst for oxygen reduction reaction in polymer electrolyte membrane fuel cell, *J. Power Sources*, 2011, **196**, 5240–5249.

30 M. Oezaslan, M. Heggen and P. Strasser, Size-Dependent Morphology of Dealloyed Bimetallic Catalysts: Linking the Nano to the Macro Scale, *J. Am. Chem. Soc.*, 2012, **134**, 514–524.

31 M. Oezaslan, F. Hasché and P. Strasser, *In Situ* Observation of Bimetallic Alloy Nanoparticle Formation and Growth Using High-Temperature XRD, *Chem. Mater.*, 2011, **23**, 2159–2165.

32 M. Pourbaix, *Atlas of Electrochemical Equilibria in Aqueous Solutions*, Nat'L Assoc. of Corrosion, Oxford, New York, 1974.

33 J. Chivot, L. Mendoza, C. Mansour, T. Pauporté and M. Cassir, New insight in the behaviour of Co–H_2O system at 25–150 °C, based on revised Pourbaix diagrams, *Corros. Sci.*, 2008, **50**, 62–69.

34 F. H. B. Lima, J. F. R. de Castro, L. G. R. A. Santos and E. A. Ticianelli, Electrocatalysis of oxygen reduction on carbon-supported Pt–Co nanoparticles with low Pt content, *J. Power Sources*, 2009, **190**, 293–300.

35 K. J. J. Mayrhofer, V. Juhart, K. Hartl, M. Hanzlik and M. Arenz, Adsorbate-Induced Surface Segregation for Core–Shell Nanocatalysts, *Angew. Chem., Int. Ed.*, 2009, **48**, 3529–3531.

36 W. A. Badawy, F. M. Al-Kharafi and J. R. Al-Ajmi, Electrochemical behaviour of cobalt in aqueous solutions of different pH, *J. Appl. Electrochem.*, 2000, **30**, 693–704.

37 I. G. Casella and M. R. Guascito, Anodic electrodeposition of conducting cobalt oxyhydroxide films on a gold surface. XPS study and electrochemical behaviour in neutral and alkaline solution, *J. Electroanal. Chem.*, 1999, **476**, 54–63.

38 S. R. Brankovic, Electrochemical Deposition as Surface Controlled Phenomenon: Fundamentals and Applications, *J. Electrochem. Soc.*, 2016, **163**, Y21.

39 N. Schubert, M. Schneider and A. Michealis, The mechanism of anodic dissolution of cobalt in neutral and alkaline electrolyte at high current density, *Electrochim. Acta*, 2013, **113**, 748–754.

40 J. B. Gerken, J. G. McAlpin, J. Y. C. Chen, M. L. Rigsby, W. H. Casey, R. D. Britt and S. S. Stahl, Electrochemical Water Oxidation with Cobalt-Based Electrocatalysts from pH 0–14: The Thermodynamic Basis for Catalyst Structure, Stability, and Activity, *J. Am. Chem. Soc.*, 2011, **133**, 14431–14442.

41 A. Minguzzi, F.-R. F. Fan, A. Vertova, S. Rondinini and A. J. Bard, Dynamic potential–pH diagrams application to electrocatalysts for water oxidation, *Chem. Sci.*, 2012, **3**, 217–229.

42 J. Chen and A. Selloni, First Principles Study of Cobalt (Hydr) oxides under Electrochemical Conditions, *J. Phys. Chem. C*, 2013, **117**, 20002–20006.

43 T. R. Jayaraman, V. K. Venkatesan and H. V. K. Udupa, Cyclic voltammetric studies of electroless cobalt in NaOH, *Electrochim. Acta*, 1975, **20**, 209–213.

44 D. Totir, Y. Mo, S. Kim, M. R. Antonio and D. A. Scherson, *In Situ* Co K-Edge X-Ray Absorption Fine Structure of Cobalt

Hydroxide Film Electrodes in Alkaline Solutions, *J. Electrochem. Soc.*, 2000, **147**, 4594.

45 L. Gragnaniello, S. Agnoli, G. Parteder, A. Barolo, F. Bondino, F. Allegretti, S. Surnev, G. Granozzi and F. P. Netzer, Cobalt oxide nanolayers on Pd(100): The thickness-dependent structural evolution, *Surf. Sci.*, 2010, **604**, 2002–2011.

46 K. M. Ismail and W. A. Badawy, Electrochemical and XPS investigations of cobalt in KOH solutions, *J. Appl. Electrochem.*, 2000, **30**, 1303–1311.

47 Y. Gauthier, Y. Joly and R. Baudoing, Surface-sandwich segregation on nondilute bimetallic alloys: $Pt_{50}Ni_{50}$ and $Pt_{78}Ni_{22}$ probed by low-energy electron diffraction, *Phys. Rev. B: Condens. Matter Mater. Phys.*, 1985, **31**, 6216–6218.

48 Y. Gauthier, Pt-metal alloy surfaces: Systematic trends, *Surf. Rev. Lett.*, 1996, **3**, 1663–1689.

49 U. Bardi, A. Atrei, E. Zanazzi, G. Rovida and P. N. Ross, Study of the reconstructed (001) surface of the $Pt_{80}Co_{20}$ alloy, *Vacuum*, 1990, **41**, 437–440.

50 M. Heggen, M. Oezaslan, L. Houben and P. Strasser, Formation and Analysis of Core-Shell Fine Structures in Pt Bimetallic Nanoparticle Fuel Cell Electrocatalysts, *J. Phys. Chem. C*, 2012, **116**, 19073–19083.

51 X. Chen, I. T. McCrum, K. A. Schwarz, M. J. Janik and M. T. M. Koper, Co-adsorption of Cations as the Cause of the Apparent pH Dependence of Hydrogen Adsorption on a Stepped Platinum Single-Crystal Electrode, *Angew. Chem., Int. Ed. Engl.*, 2017, **56**, 15025–15029.

52 I. T. McCrum and M. J. Janik, pH and Alkali Cation Effects on the Pt Cyclic Voltammogram Explained Using Density Functional Theory, *J. Phys. Chem. C*, 2016, **120**, 457–471.

53 X. Yang, J. Nash, N. Oliveira, Y. Yan and B. Xu, Understanding the pH Dependence of Underpotential Deposited Hydrogen on Platinum, *Angew. Chem., Int. Ed. Engl.*, 2019, **58**(49), 17718–17723.

54 F. Şen and G. Gökağaç, Different Sized Platinum Nanoparticles Supported on Carbon: An XPS Study on These Methanol Oxidation Catalysts, *J. Phys. Chem. C*, 2007, **111**, 5715–5720.

55 A. P. Grosvenor, S. D. Wik, R. G. Cavell and A. Mar, Examination of the bonding in binary transition-metal monophosphides MP (M = Cr, Mn, Fe, Co) by X-ray photoelectron spectroscopy, *Inorg. Chem.*, 2005, **44**, 8988–8998.

56 N. S. McIntyre and M. G. Cook, X-ray photoelectron studies on some oxides and hydroxides of cobalt, nickel, and copper, *Anal. Chem.*, 1975, **47**, 2208–2213.

57 D. B. Mitton, J. Walton and G. E. Thompson, An XPS and AES study of the ageing of a Co–20%Ni metal-evaporated tape, *Surf. Interface Anal.*, 1993, **20**, 36–42.

58 T. L. Barr, An ESCA study of the termination of the passivation of elemental metals, *Journal of Physical Chemistry*, 1978, **82**, 1801–1810.

59 J. Yang, H. Liu, W. N. Martens and R. L. Frost, Synthesis and Characterization of Cobalt Hydroxide, Cobalt Oxyhydroxide, and Cobalt Oxide Nanodiscs, *J. Phys. Chem. C*, 2010, **114**, 111–119.

60 D. Briggs and V. A. Gibson, Direct observation of multiplet splitting in 2P photoelectron peaks of cobalt complexes, *Chem. Phys. Lett.*, 1974, **25**, 493–496.

61 M. C. Biesinger, B. P. Payne, A. P. Grosvenor, L. W. M. Lau, A. R. Gerson and R. S. C. Smart, Resolving surface chemical states in XPS analysis of first row transition metals, oxides and hydroxides: Cr, Mn, Fe, Co and Ni, *Appl. Surf. Sci.*, 2011, **257**, 2717–2730.

62 M. Chatti, J. L. Gardiner, M. Fournier, B. Johannessen, T. Williams, T. R. Gengenbach, N. Pai, C. Nguyen, D. R. MacFarlane, R. K. Hocking and A. N. Simonov, Intrinsically stable *in situ* generated electrocatalyst for long-term oxidation of acidic water at up to 80 °C, *Nat. Catal.*, 2019, **2**, 457–465.

63 J. S. Mondschein, J. F. Callejas, C. G. Read, J. Y. C. Chen, C. F. Holder, C. K. Badding and R. E. Schaak, Crystalline Cobalt Oxide Films for Sustained Electrocatalytic Oxygen Evolution under Strongly Acidic Conditions, *Chem. Mater.*, 2017, **29**, 950–957.

64 M. Huynh, T. Ozel, C. Liu, E. C. Lau and D. G. Nocera, Design of template-stabilized active and earth-abundant oxygen evolution catalysts in acid, *Chem. Sci.*, 2017, **8**, 4779–4794.

65 G. W. Sievers, A. W. Jensen, J. Quinson, A. Zana, F. Bizzotto, M. Oezaslan, A. Dworzak, J. J. K. Kirkensgaard, T. E. L. Smitshuysen, S. Kadkhodazadeh, M. Juelsholt, K. M. Ø. Jensen, K. Anklam, H. Wan, J. Schäfer, K. Čépe, M. Escudero-Escribano, J. Rossmeisl, A. Quade, V. Brüser and M. Arenz, Self-supported Pt–CoO networks combining high specific activity with high surface area for oxygen reduction, *Nat. Mater.*, 2020, **20**, 208–213.

66 M. L. Perry, T. W. Patterson and C. Reiser, Systems strategies to mitigate carbon corrosion in fuel cells, *ECS Trans.*, 2006, **3**, 783–795.

67 J. Kim, J. Lee and Y. Tak, Relationship between carbon corrosion and positive electrode potential in a proton-exchange membrane fuel cell during start/stop operation, *J. Power Sources*, 2009, **192**(2), 674–678.

68 W. K. Behl and J. E. Toni, Anodic oxidation of cobalt in potassium hydroxide electrolytes, *J. Electroanal. Chem. Interfacial Electrochem.*, 1971, **31**, 63–75.

69 B. S. Yeo and A. T. Bell, Enhanced Activity of Gold-Supported Cobalt Oxide for the Electrochemical Evolution of Oxygen, *J. Am. Chem. Soc.*, 2011, **133**, 5587–5593.

70 M. Bajdich, M. García-Mota, A. Vojvodic, J. K. Nørskov and A. T. Bell, Theoretical Investigation of the Activity of Cobalt Oxides for the Electrochemical Oxidation of Water, *J. Am. Chem. Soc.*, 2013, **135**, 13521–13530.